

VALIDATING SEMI-ANALYTIC MODELS OF HIGH-REDSHIFT GALAXY FORMATION USING RADIATION HYDRODYNAMICAL SIMULATIONS

BENOIT CÔTÉ,^{1,2,3,4} DEVIN W. SILVIA,^{5,6,7} BRIAN W. O'SHEA,^{1,5,6,3} BRITTON SMITH,⁸ AND JOHN H. WISE⁹

¹*National Superconducting Cyclotron Laboratory, Michigan State University, MI, 48823, USA*

²*Konkoly Observatory, Research Centre for Astronomy and Earth Sciences, Hungarian Academy of Sciences, Konkoly Thege Miklos ut 15-17, H-1121 Budapest, Hungary*

³*Joint Institute for Nuclear Astrophysics - Center for the Evolution of the Elements, USA*

⁴*NuGrid Collaboration, <http://nugridstars.org>*

⁵*Department of Physics and Astronomy, Michigan State University, MI, 48823, USA*

⁶*Department of Computational Mathematics, Science and Engineering, Michigan State University, MI, 48823, USA*

⁷*National Science Foundation, Astronomy and Astrophysics Postdoctoral Fellow, USA*

⁸*San Diego Supercomputer Center, University of California, San Diego, CA 92093, USA*

⁹*Center for Relativistic Astrophysics, Georgia Institute of Technology, 837 State Street, Atlanta, GA 30332, USA*

Submitted to ApJ

ABSTRACT

We use a cosmological hydrodynamic simulation calculated with **Enzo** and the semi-analytic galaxy formation model (SAM) **GAMMA** to address the chemical evolution of dwarf galaxies in the early universe. The long-term goal of the project is to better understand the origin of metal-poor stars and the formation of dwarf galaxies and the Milky Way halo by cross-validating these theoretical approaches. We combine **GAMMA** with the merger tree of the most massive galaxy found in the hydrodynamic simulation and compare the star formation rate, the metallicity distribution function (MDF), and the age-metallicity relationship predicted by the two approaches. We found that the SAM can reproduce the global trends of the hydrodynamic simulation. However, there are degeneracies between the model parameters and more constraints (e.g., star formation efficiency, gas flows) need to be extracted from the simulation to isolate the correct semi-analytic solution. Stochastic processes such as bursty star formation histories and star formation triggered by supernova explosions cannot be reproduced by the current version of **GAMMA**. Non-uniform mixing in the galaxy's interstellar medium, coming primarily from self-enrichment by local supernovae, causes a broadening in the MDF that can be emulated in the SAM by convolving its predicted MDF with a Gaussian function having a standard deviation of ~ 0.2 dex. We found that the most massive galaxy in the simulation retains nearly 100% of its baryonic mass within its virial radius, which is in agreement with what is needed in **GAMMA** to reproduce the global trends of the simulation.

Keywords: galaxies: high-redshift — galaxies: formation — galaxies: star formation — stars: abundances

1. INTRODUCTION

The hierarchical nature and physical complexity of galaxy formation makes it challenging to create physically realistic and computationally tractable models that incorporate all stages of a galaxy’s history, from the very first stars to the present day. A further layer of difficulty arises from the fact that observations of the early universe via campaigns such as the Hubble Ultra-Deep Field and the Hubble Frontier Fields (e.g., Williams et al. 1996; Beckwith et al. 2006; Illingworth et al. 2013; Atek et al. 2014; Ishigaki et al. 2015) tend to measure different and less detailed quantities than observations of the Milky Way and its neighbors galaxies (Frebel & Norris 2015; Bland-Hawthorn & Gerhard 2016). As a result, using observations to inform the models is a non-trivial endeavour. In this paper, we present the first steps toward developing reliable chemical evolution models for the early universe, using high-redshift cosmological hydrodynamic simulations of galaxy formation to calibrate them.

Theoretical studies of galaxy formation typically take one of two approaches to build upon analytic efforts, each of which has its own strengths and limitations. The first approach uses cosmological simulations that employ as much physics as is computationally tractable and typically include dark matter dynamics, (magneto)hydrodynamics, plasma heating microphysics, cooling, chemistry, sub-grid prescriptions for star formation and stellar feedback, and, to a greater extent in the modern era than in the past, radiation transport, cosmic rays, and additional plasma processes. This method has been successful in reproducing many of the observable properties of low- and high-redshift (z) galaxies (e.g., Vogelsberger et al. 2014; Hopkins et al. 2014; Chen et al. 2014; Wise et al. 2014; Schaye et al. 2015; Agertz & Kravtsov 2016).

However, due to the costs and challenging nature of the computations, an individual simulation must make compromises in the implemented physics, the dynamic range in resolution, and/or in the number of distinct galaxies simulated. This typically means that an individual calculation either models galaxies in the high-redshift universe at very high spatial resolution with complex physics, a small number of low-redshift galaxies at reasonably good spatial resolution with less sophisticated physics, or many low-redshift galaxies at moderate spatial resolution with similarly reduced physics. Such compromises are necessary given the finite computational resources, but they make predictions regarding the full range of stellar populations within the Local Group impossible from individual simulations. Calculations that can reach $z = 0$ have mass and spatial resolu-

tions that are too poor to adequately resolve the earliest generations of galaxy formation. Moreover, the high computational cost of each simulation prevents exploring variations in parameters and physical processes in a thorough way.

The second approach to the theoretical study of galaxy formation is to use semi-analytical models (SAMs). These models use merger trees based on either the extended Press-Schechter formalism or on dark matter cosmological simulations to capture the hierarchical nature of structure formation. The latter method gained in popularity in recent years due to its native inclusion of spatial and kinetic information in addition to mass and formation history. Various physical prescriptions such as star formation, stellar feedback, and gas flows are layered on top of these merger trees and are represented as sets of coupled ordinary differential equations. The output of these models are typically compared to the observable properties of low-redshift galaxies. We refer to Baugh (2006) and Somerville & Davé (2015) for a more general discussion on SAMs of galaxy formation.

This approach has been used several times in the past to address the chemical evolution of galaxies as a function of their mass (e.g., Yates et al. 2013; Croton et al. 2016; Fontanot et al. 2017) as well as the chemical evolution of specific galaxies such as the Milky Way (e.g., Komiya et al. 2014; Crosby et al. 2016), local dwarf spheroidal and ultrafaint galaxies (e.g., Romano & Starkenburg 2013; Starkenburg et al. 2013; Romano et al. 2015), and the stellar halo (e.g., Tumlinson 2006, 2010). The strength of SAMs is their low computational cost that facilitates the exploration of parameter spaces and physical processes, which has been done in recent years using a variety of statistically-robust methods including both Bayesian and frequentist Markov Chain Monte Carlo, as well as Bayesian Emulators (e.g., Lu et al. 2012; Henriques et al. 2013; Rodrigues et al. 2017). But their weakness is the treatment of those physical processes, which are more abstract and simplified compared to the physics-rich simulations described above. Since the physical processes are not directly modelled and resolved, it can be difficult to trust the outputs of SAMs and to understand the degeneracies between their parameters.

Observationally, metal-poor stars found in dwarf galaxies and in the halo of the Milky Way and Andromeda are Local Group tracers of the first generations of star formation. The study of these old stellar populations, often called “Galactic Archaeology,” provides a glimpse into the distant past by assuming that (1) metal-poor stars are temporally and nucleosynthetically close to the first galaxies that formed in the early universe,

and thus can be used to infer their properties; and (2) stellar halos and dwarf galaxies are relatively clean remnants of the early hierarchical assembly era of structure formation, with ultra-faint galaxies being particularly pristine environments for the study of the early universe (Bovill & Ricotti 2009; Somerville & Davé 2015; Boylan-Kolchin et al. 2015; Weisz & Boylan-Kolchin 2017). However, confronting observations of metal-poor stars with theoretical models results in several distinct challenges. Ultra-faint dwarf satellite galaxies in particular are a challenging environment to model in the same simulations as the massive galaxies that they orbit due to their small mass and shallow potential wells, and thus the huge dynamical ranges required. Their stellar populations are particularly susceptible to formation environment and to being removed from the galaxies via tidal harassment, particularly if poorly resolved spatially and/or in terms of dark matter particle mass.

At present, it is not possible to run physics-rich simulations of a Milky Way-type galaxy that include the dynamic range in space and mass required to adequately resolve the formation of ultra-faint dwarfs. A different theoretical approach is thus necessary. The obvious solution is to use SAMs, which provide the necessary dynamic range. But the fundamental challenge with applying SAMs to this problem is that their physical prescriptions are often calibrated by comparison to observations of massive and low-redshift galaxies ($L_{\text{gal}} \gtrsim L_{\text{MW}}$, $z_{\text{obs}} \lesssim 1$), though in recent years this has been extended to substantially higher redshifts and to lower-mass galaxies (see, e.g., Henriques et al. 2015; Lacey et al. 2016; Rodrigues et al. 2017). The applicability of the physical prescriptions and input parameters that are chosen is therefore questionable for extremely high-redshift, very low-mass galaxy formation (e.g., Bower et al. 2006; Kim et al. 2009; Bower et al. 2010). In addition, direct observations of high-redshift galaxies are limited.

There is a path forward that will allow us to more reliably use semi-analytic models as theoretical tools for Galactic Archaeology and for the exploration of galaxy formation and evolution in the early universe. Rather than calibrating SAMs with galaxy observations at low redshift, we propose to calibrate them using physics-rich galaxy formation simulations and low-metallicity stellar populations observed in the Local Group dwarfs. The theoretical aspect of this calibration can use merger trees derived directly from the selected hydrodynamic simulations. Detailed analysis of the properties of these calculations can provide valuable insights into the robustness of the SAM prescriptions and lead to the creation of new prescriptions that are more appropriate for low-

mass, high-redshift galaxies. Observations of the ultra-faint dwarf galaxies can calibrate the models in a complementary way, by helping to resolve model parameter degeneracies.

This paper presents the first step in this process, building on our expertise in both semi-analytical modeling of galaxy formation and in physics-rich cosmological simulations (Wise et al. 2012a, 2014; Côté et al. 2015; O’Shea et al. 2015; Côté et al. 2016a; Xu et al. 2016; Côté et al. 2017a,b). We present a new SAM for galaxy formation and chemical evolution, **GAMMA**, and compare it to the cosmological hydrodynamic simulation of high-redshift galaxy formation used in Wise et al. (2012a, 2014).

The outline of this paper is as follows. In Section 2, we precisely define the experiment pursued in this paper. In Section 3, we summarize the **Enzo** simulations used as a baseline for comparison with our SAM, and in Section 4, we introduce **GAMMA**, our semi-analytic chemical evolution code. In Section 5, we compare the predictions of the two types of models, and in Sections 6 and 7, we discuss extensions to the baseline model that must be made to improve agreement and degeneracies in the SAM parameters, respectively. We then discuss some limitations and implications of this work in Section 8, and summarize our results in Section 9.

2. DEFINING THE EXPERIMENT

In this paper, we experiment with the use of multi-physics cosmological simulations as a tool to calibrate semi-analytic models of galaxy formation for galaxies in the early universe that should be observable by the James Webb Space Telescope ($M_{\text{vir}} \sim 10^9 M_{\odot}$, $z \sim 7 - 8$), although it may require gravitationally-lensed fields equivalent to the Hubble Frontier Fields to do so (see, e.g., O’Shea et al. 2015). We determine the formation history for the most massive galaxy in our simulation at the calculation’s stopping redshift ($z = 7.29$) by using many simulation outputs to create a merger tree that encompasses all dark matter halos at earlier times which could plausibly form stars, and then use this merger tree as an input for our semi-analytic model. This eliminates the galaxy’s growth history as a source of uncertainty in our inter-model comparison, and allows us to focus on the physical prescriptions used in the semi-analytic model as well as the model’s other input parameters. We then ask two fundamental questions:

1. Using our standard semi-analytic galaxy formation model (which is similar to other models of its type), how closely are we able to match the galaxy’s star formation history and metallicity dis-

tribution function, as measured at the final redshift in the simulation?

2. What key qualities of the multiphysics simulations are absent from the approximations made in the semi-analytical model, and how does a more complete incorporation of these qualities affect the predictions made by the model?

The first question is important because the star formation history and MDF are two of the primary observable properties of low-mass galaxies (e.g., Local Group dwarf galaxies), with more detailed physical properties either being difficult to determine or possibly contaminated by interaction with other, more massive galaxies (e.g., structural information about the stellar populations can be difficult to infer due to small numbers of stars, and can be modified by tidal harassment from the central galaxy). We examine this question in Section 5.

The second question is important because the level of abstraction in the multiphysics simulations is much different than in the semi-analytic models, and thus it is possible to find emergent properties of these simulations that can inform the semi-analytic models. Put somewhat differently, multiphysics simulations emulate the universe at a relatively fine level of granularity by modeling dark matter dynamics, hydrodynamics, radiation transport, the heating and cooling of gas, and star formation and feedback in many individual resolution elements that are much smaller than the scale of individual galaxies. This allows phenomena like starbursts, accretion of gas, and galactic winds to develop naturally via interactions of these individual physical processes. Semi-analytic models of galaxy formation, on the other hand, typically model galaxy evolution by describing physical phenomena such as star formation or galactic winds using sets of ordinary differential equations that depend on bulk galaxy quantities such as the mass of gas and stars in the galaxy and the virial mass of the dark matter halo where the baryons reside. Given these different levels of abstraction, a close examination of the multiphysics simulations of low-mass galaxies may show physical behaviors that are not captured in the standard semi-analytic models (in particular, behaviors relating to the rate of mixing of metal-enriched gas, the relatively shallow potential wells of small dark matter halos, and the rapid evolution of cosmological structure in the early universe) that can be used to increase the physical realism, and thus predictive capabilities, of the semi-analytic model. We examine this question in Sections 6 and 7.

It is important to acknowledge that the interpretation of the experiment undertaken in this paper is com-

plicated by the fact that we are using one theoretical framework (multiphysics simulations) to inform a second, substantially different theoretical framework (semi-analytic models). Both of these theoretical frameworks have significant implicit and explicit assumptions built into them that may impact their realism and predictive power, and thus comparing them may introduce systematic errors. In addition, it is dangerous to assume that multiphysics simulations (our baseline for comparison) behave in a way that is actually “true.” (Note that these ideas are explored more thoroughly in Section 8). However, in the absence of an abundance of observational data of low-mass, high redshift galaxies, this is the only practical means of improving the physical accuracy of our semi-analytic models.

3. HYDRODYNAMIC SIMULATION

3.1. *The Enzo Code*

The simulation described in Section 3.2 is calculated using the **Enzo** adaptive mesh refinement code (Bryan et al. 2014). **Enzo** uses an N-body adaptive particle-mesh solver to model the dark matter dynamics, and solves the equations of hydrodynamics using the second-order-accurate piecewise parabolic method (PPM) and the HLLC Riemann solver (Woodward & Colella 1984; Bryan & Norman 1997; Bryan et al. 1995; Toro 1997). **Enzo** uses the Berger and Colella block-structured adaptive mesh refinement scheme in Cartesian coordinates (Berger & Colella 1989). This simulation also includes **Enzo**’s nine-species non-equilibrium chemistry and cooling model, which follows species of H, He, and H₂ (Abel et al. 1997; Anninos et al. 1997) and includes the H₂ cooling rates from Glover & Abel (2008). It also uses the **Moray** radiation transport package (Wise & Abel 2011) and “star particles” to represent both individual Population III stars and ensembles of metal-enriched stars.

3.2. *Simulations*

The simulation used in this paper is the “RP” simulation described in great detail in Wise et al. (2012a, 2014, with this calculation hereafter referred to as the “W12” simulation), but we repeat the most important details here. The calculation uses a simulation box that is 1 Mpc (comoving) on a side with a 256^3 root grid and 256^3 dark matter particles. This gives a dark matter mass resolution of $1,840 M_{\odot}$, which is enough to resolve halos with masses exceeding $\simeq 2 \times 10^5 M_{\odot}$. The initial conditions were generated at $z = 130$ using the **grafic** package (Bertschinger 2001) and the seven-year WMAP best-fit parameters (Komatsu et al. 2011): $\Omega_M = 0.266$, $\Omega_{\Lambda} = 0.734$, $\Omega_b = 0.0449$, $h = 0.71$, $\sigma_8 = 0.81$, and $n = 0.963$.

The simulation was evolved from $z = 140$ to $z = 7.29$ using the physics described in Section 3.1 and a maximum of $N_{\text{ref}} = 12$ levels of refinement, giving a co-moving resolution of 0.95 pc at the highest level. Cells were refined based on dark matter and baryon mass in a super-Lagrangian (i.e., increasingly aggressive) manner, and always resolve the Jeans length by a minimum of 4 cells to avoid artificial fragmentation during the collapse of gas clouds (Truelove et al. 1998). Both Population III and metal-enriched stars were formed, with Pop III stars having a top-heavy IMF and metal-enriched stars having a more standard Galactic-like Salpeter IMF. Gas collapsing in cells with metallicities $[Z/H]^1 < -4$ form a single Population III star whose mass is drawn from a top-heavy IMF that is a power-law above $100 M_{\odot}$ and is exponentially damped below that mass; more metal-enriched gas forms a star particle representing an ensemble of metal-enriched stars. All star particles feedback radiation using the MORAY radiation transport algorithm and mass, metals, and thermal energy through supernova explosions.

3.3. Analysis

The key data product required from a cosmological simulation for use in semi-analytic models is a halo merger tree. We generate this by using the `Rockstar` phase-space halo finder (Behroozi et al. 2013b) on the simulation’s dark matter particles at every simulation data output, which produces a halo catalog composed of all of the gravitationally-bound dark matter halos and sub-halos in the simulation. We then used the `consistent-trees` tool (Behroozi et al. 2013c) to create a gravitationally self-consistent merger tree for every halo in the simulation at $z = 7.29$ (the last simulation data output). To load the output from `consistent-trees` and step through the halos in a given tree, we use the `ytree`² code (Smith 2018), an extension of the `yt`³ analysis toolkit (Turk et al. 2011) designed for the ingestion and manipulation of merger tree data from multiple sources. The `ytree` code provides a Python interface for merger tree-like data structures, allowing the user to easily traverse from a halo to its ancestors or descendants, to access field data with symbolic units for a partial or whole tree, to add new fields resulting from further analysis, and to save a tree or group of trees to optimized, reloadable format.

In this work, we use the definitions provided by `Rockstar` for basic halo properties, such as position,

virial radius (R_{vir}), and virial mass (M_{vir}). These are described in detail in Behroozi et al. (2013b), but we present them briefly here. A halo’s position is defined as the center of mass of a central subgroup of N particles for which the Poisson error, expressed as σ/\sqrt{N} , is minimized. Virial masses and radii are defined as the properties of a sphere within which the average density is equal to the threshold overdensity given in Bryan & Norman (1998).

3.4. Separating Star Particles

Star particles found inside the virial radius of the main galaxy at the final redshift can have different origins. They might have formed in the main galaxy or in the infalling satellite galaxies, but they could also have been ejected from neighbouring galaxies. Since we aim to reproduce the evolution of individual galaxies with `GAMMA` using their merger tree, we need to separate and tag each star particle in order to recover their specific star formation history and metallicity distribution function.

Using `ytree`, we first identify the most massive progenitors of the main and satellite halos and record their virial radius R_{vir} and the coordinate of their center of mass \vec{r}_0 as a function of redshift. Then, for each redshift from the highest to the lowest, we identify all star particles that formed between the previous and current redshift. For each *new* star particle j , we calculate its normalized distance from the center of each halo i ,

$$d_{j,i} = \frac{|\vec{r}_j - \vec{r}_{0,i}|}{R_{\text{vir},i}}, \quad (1)$$

where all quantities vary as a function of redshift, and \vec{r}_j is the current position of the particle j . Each star particle is then associated with the halo showing the minimum $d_{j,i}$ value. Using this approach, we found that the most massive progenitors of the main halo and its most massive satellite (pink circle in Figure 1) allow to recover 97.4% the stellar content found inside the main halo at the final redshift, which is sufficient for the purpose of this work.

3.5. Galaxy Behaviour

In this paper, we focus our attention on the most massive galaxy in the simulation – the same galaxy targeted in the W12 simulation. This galaxy, henceforth referred to as the “target galaxy,” has a range of interesting physical features. Figures 1 through 4 show some of the large-scale properties of the target halo, which are also generally representative of high-redshift galaxy formation. Note that by the end of the simulation, the main halo and its two satellites have a total (dark matter plus baryon) mass of $5.45 \times 10^8 M_{\odot}$, and 1.30×10^8 and $1.11 \times 10^8 M_{\odot}$, respectively.

¹ $[Z/H] \equiv \log_{10}(Z/H) - \log_{10}(Z/H)_{\odot}$

² <http://ytree.readthedocs.io/>

³ <http://yt-project.org/>

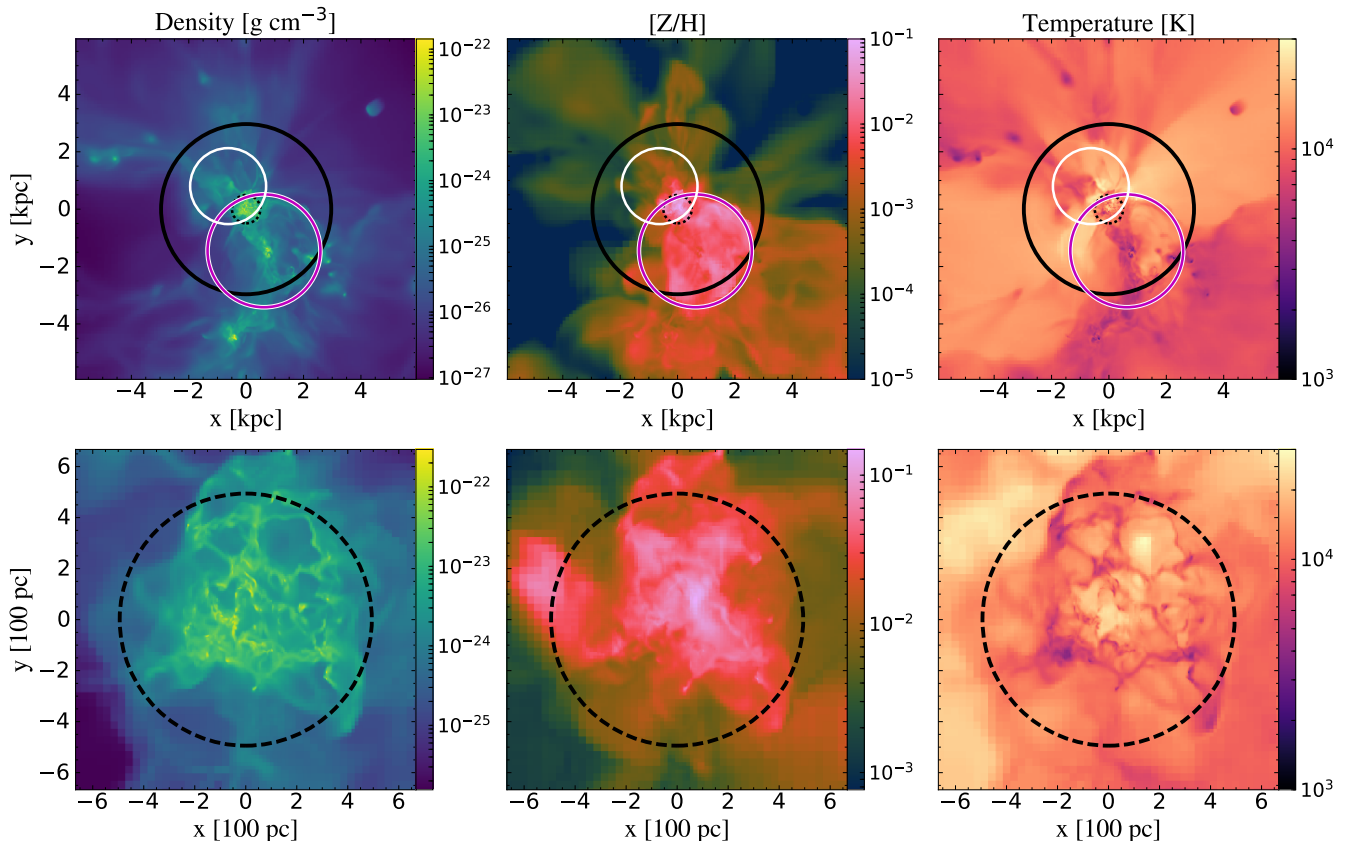


Figure 1. Snapshots at $z = 7.45$ of the density (left column), metallicity (middle column), and temperature (right column) for the most massive galaxy in the simulation. All panels consist of projections weighted by density. Values for metallicities are normalized to $Z_{\odot} = 0.014$. **Top row:** The solid and dashed black circles trace the virial and inner radius of the main halo, respectively. The radius of the inner region is set to a sixth of the virial radius. The solid pink and white circles trace the virial radius of two satellite halos that have not merged by the end of the simulation. **Bottom row:** Same as in the top panels, but zoomed on the inner region. By the end of the simulation, the main halo and its two satellites have a total (dark matter plus baryon) mass of $5.45 \times 10^8 M_{\odot}$, and 1.30×10^8 (pink) and 1.11×10^8 (white) M_{\odot} , respectively.

Figure 1 shows density-weighted projections at $z = 7.45$ of the density field, metallicity, and temperature for the target galaxy, at two physical scales: out to roughly twice the virial radius of the target galaxy, and in the central star-forming region of the same galaxy. These images were chosen to be at this redshift rather than the final redshift to highlight the complexity of the baryonic structure at all scales within the galaxy. Clear filamentary structure and substantial inhomogeneity in metallicity can be seen in the halo outside of the star-forming region, with the regions of highest metallicity relating to infalling satellite halos rather than metal-enriched galactic outflows (although those are also present, but correlated more strongly with high temperatures due to the accompanying radiation from massive stars).

The central star-forming region has gas at a wide variety of densities and temperatures, and displaying a range of metallicities. While this is in some ways analogous to the interstellar media in galaxies like the Milky

Way, the range of observed temperatures is much smaller due to the substantially lower virial temperature of the halo (tens of thousands of Kelvin rather than millions of Kelvin). Broadly speaking, there are several different dense regions of star formation that have differing metallicities, rather than a single molecular-cloud like structure that one would expect in, e.g., Population III star formation (Abel et al. 2002; Bromm et al. 2002; O’Shea & Norman 2007; Turk et al. 2009). In addition, evidence of stellar feedback can be seen in the hot, low density, metal-enriched gas in the central regions that are spatially adjacent to star-forming regions.

Figure 2 shows the star formation history (SFH) of both the target halo and its most massive satellite halo, smoothed on a 2 Myr time scale. All stars included in this figure are formed in the main progenitor halos of the target and satellite galaxies (see Section 3.4). Overall, the SFH of the target halo displays a steadily increasing trend with time, although both halos show substan-

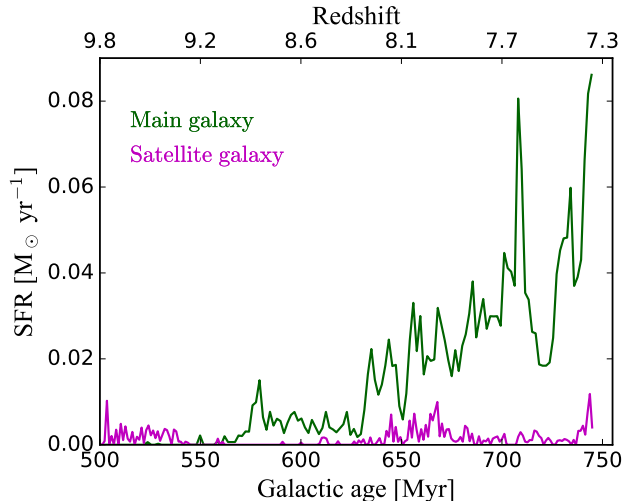


Figure 2. Star formation history of the target halo (green) and its most massive satellite halo (pink, also shown as the pink circles in Figure 1). The total integrated stellar mass formed in the target and satellite halo at the end of the simulation at $z = 7.29$ is 3.58×10^6 and $4.60 \times 10^5 M_{\odot}$, respectively.

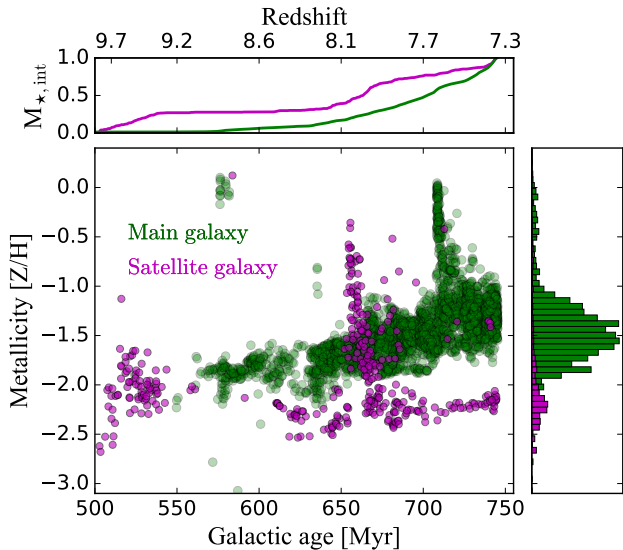


Figure 3. Main panel: Metallicity (in units of log Solar metallicity) of all stellar populations as a function of their formation time (or galactic age) for the target halo (green) and its most massive satellite halo (pink). **Top panel:** Integrated stellar mass formed as function of time, scaled to the total stellar mass in each halo at $z = 7.29$. **Left panel:** Metallicity distribution functions of all stellar populations.

tial variability in their star formation rate on short time scales. This variability is consistent with other simulations of high-redshift galaxy formation (e.g., the Renaissance simulations, [Chen et al. 2014](#); [O’Shea et al. 2015](#); [Xu et al. 2016](#)), and with the idea that low-mass galaxies

have shallow potential wells with easily-disrupted star formation. The total integrated stellar mass formed in the target and satellite halos at the end of the simulation is 3.58×10^6 and $4.60 \times 10^5 M_{\odot}$, respectively.

Figure 3 shows the metallicity of each “star particle” (i.e., each specific particle tracing the formation of a parcel of stars) in the target halo and its most massive satellite as a function of formation time, with sub-panels displaying the cumulative star formation history and the metallicity distribution function of the stars in each galaxy. As with Figure 2, this includes stars formed in all of the progenitor halos of each of the two galaxies at a given point in time. This plot displays several notable features. First, while the metallicity of stars formed in the target halo and its progenitors trends upward, there is substantial variation in stellar metallicity at any given time. This is due to the variation in metallicity of star-forming regions within the galaxy due to non-uniform mixing. There are “spikes” in Figure 3 corresponding to relatively extremely metal-rich star formation at $t \simeq 575$ Myr and 720 Myr in the main galaxy. Those stellar populations formed out of relatively unmixed gas containing a large fraction of nearby supernova ejecta. Their formation is likely triggered by the short cooling timescales of the hot metal-rich gas phase (see Section 8.4), rather than by galaxy merger events.

The satellite halo (purple dots) does not display the same trend of increasing metallicity with time - rather, its progenitors are more metal-rich at early times, and have approximately constant stellar metallicity for 200 Myr afterward with the exception of a large metallicity spike at $t \simeq 660$ Myr. This may be related to the different formation histories of these objects, and to their difference in size - metallicity is determined by a wide variety of factors, including the production of metal-enriched gas by supernovae, the outflow of metal-enriched gas from the halo driven by supernovae, and the inflow of gas of different metallicity from the cosmic web and infalling satellites (with the infalling satellites possibly having highly metal-enriched gas in this particular instance, as can be seen in Figure 1).

Figure 4 shows snapshots of the baryon density and metallicity of the target galaxy at $z = 8.64, 8.24, 7.88,$ and 7.66 , with the frame of the image extending to roughly three virial radii. As with Figure 1, this sequence of images shows the complexity of the circumgalactic environment for the target galaxy and its satellites. The target galaxy is accreting matter from roughly three different filaments, with a tremendous amount of metal entering into the circumgalactic environment due to the approach of the massive satellite (bottom-right

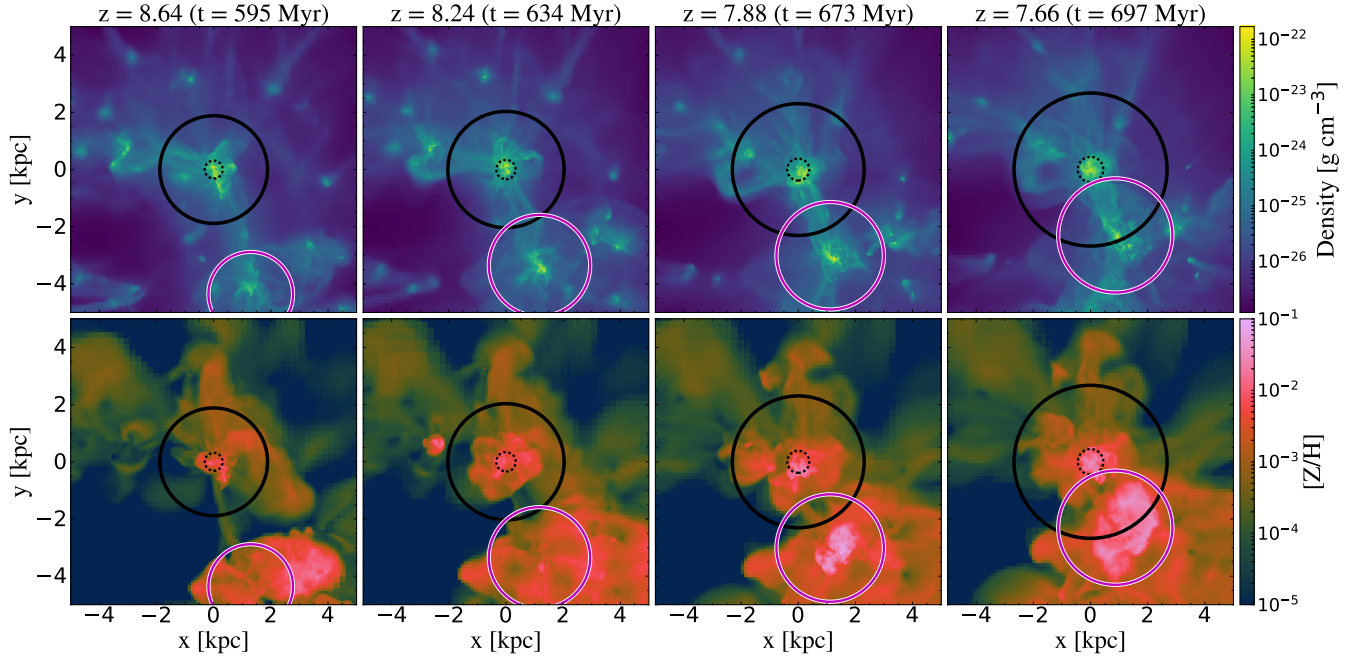


Figure 4. Evolution of the density (top row) and metallicity (bottom row) as a function of galactic age (from left to right) for the most massive galaxy in the simulation (the “target galaxy”), shown as density-weighted projections. The radius of the solid and dotted black circles represent the virial radius of the target halo and a sixth of that radius, respectively. The radius of the pink circle represents the virial radius of the most massive satellite.

corner), which is surrounded by a large cloud of metal-enriched gas originating from a recent burst of supernovae. This burst is associated with the metal-rich stellar populations shown in Figure 3 (the pink metallicity spike at $t \simeq 660$ Myr). The formation of these populations in the satellite galaxy occurs before it enters the virial radius of the target galaxy, which can be seen in the two middle columns of Figure 4.

4. CHEMICAL EVOLUTION CODE

In this section we present **GAMMA** (Galaxy Assembly with Merger trees for Modeling Abundances), a semi-analytic chemical evolution code that accounts for the mass assembly history of galaxies using merger trees extracted from cosmological simulations. The novelty of **GAMMA** is its connection with nuclear astrophysics. It represents the end-point of our open-source JINA-NuGrid chemical evolution pipeline (Côté et al. 2017b). All of our codes are available online⁴.

4.1. GAMMA

The first step in using **GAMMA** is to traverse the entire halo merger tree and re-organize the tree-nodes in order to feed the properties of all galaxy mergers into **GAMMA**. In this work, we use the merger tree of the most massive

galaxy of the W12 simulation shown in Figure 5. Each tree-node refers to a unique snapshot of a halo at a specific redshift in the simulation. In **ytree**, even if a halo does not experience any merger during a certain redshift interval, the tree-nodes associated with this specific halo will still have unique entries and halo identification numbers in the merger tree. This is a consequence of the way that merger trees are created from halo catalogs (which are unique at each redshift), and is useful for obtaining accurate halo growth rates.

While traversing the merger tree, we identify all tree-nodes that are the starting point of a new *branch*, which is defined as a segment in the merger tree (or a series of interconnected tree-nodes) where no merger is occurring, although the halo may still grow by accretion from its surroundings. For each tree-node, we then move forward in time and identify all interconnected tree-nodes until we encounter a merger, which represents the end point of a branch. **GAMMA** will then consider each branch as an isolated galaxy that is not interacting with surrounding galaxies. Figure 6 illustrates this terminology using the same type of graph as Figure 5, highlighted to emphasize individual branches.

Once all branches have been identified, **GAMMA** creates every galaxy in chronological order, from the highest to the lowest redshift, using the **OMEGA+** code (see Section 4.2). Each galaxy receives the time-dependent properties of their associated branch as an input (e.g.,

⁴ <http://github.com/becot85/JINAPyCEE>

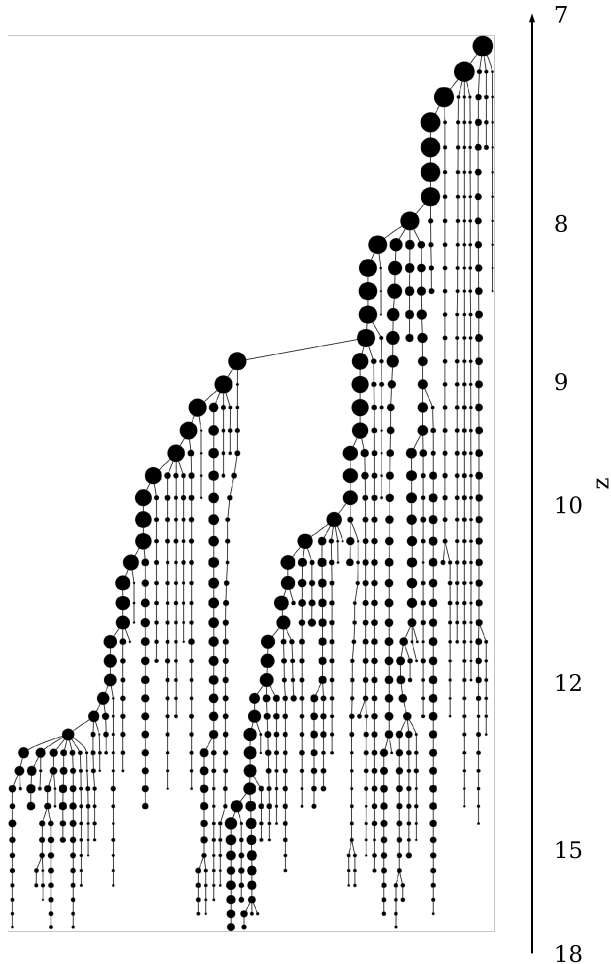


Figure 5. Merger tree of the most massive galaxy in the Wise et al. (2012a) simulation. Every progenitor halo, or tree-node, is represented by a circle where its size is proportional to the logarithm of its virial mass. The mass assembly of the galaxy can be followed in time in the upward direction up to $z = 7.29$, the final redshift of the simulation. A series of individual tree-nodes connected by a line along the redshift axis shows the mass evolution of a halo, but taken at different snapshots in time. Tree-nodes that are descending from more than one progenitor represent mergers. Only halos with masses above $10^5 M_{\odot}$ are shown.

dark matter mass growth) and is evolved until it encounters a merger with one or more galaxies. When a new galaxy is the result of a merger, GAMMA combines the stellar and gaseous components of all progenitor galaxies involved in the merger and feeds this information into OMEGA+ for the initial conditions of the new galaxy. During the process, stars formed in the progenitor galaxies stay active in the new galaxy, meaning that they will continue to inject metals and energy into their new environment.

In the present version of GAMMA, we do not account for ram pressure and tidal stripping processes of satellite galaxies that can occur when entering the dark matter halo of a central galaxy (see e.g., Simpson et al. 2017). This can modify the amount of gas and metals present in the CGM of the central galaxies in our models before the merger event between the satellite and central galaxies (see Section 7.3 for a discussion). This could also reduce the hot gas reservoir of satellite galaxies and therefore reduce their star formation rate.

4.2. OMEGA+

OMEGA+ is a galaxy evolution code that consists of a star-forming region, called the cold gas reservoir, which also is assumed to contain the stellar population in the galaxy. This is surrounded by a hot gas reservoir filling the dark matter halo of the host galaxy. For the sake of clarity, in this work we refer to the region containing cold gas and stars as the “galaxy” and the reservoir of hot gas surrounding it as the “circumgalactic medium”, or CGM. The star-forming region is simulated using the galactic chemical evolution code OMEGA (One-zone Model for the Evolution of GALaxies; Côté et al. 2017a). Given an input star formation history, this latter code calculates the chemical mixture of the galactic gas (i.e., cold gas reservoir) as a function of time by accounting for the contribution of multiple stellar populations as well as the presence of galactic inflows and outflows.

The role of OMEGA+ is to interact with OMEGA at each timestep in order to control the rates of inflow, outflow, and star formation (see equations below). Within this framework, OMEGA is thus only used to calculate the mass and energy returned by all stellar populations as a function of their initial mass, age, and metallicity. We refer to Section 4.3 for more details on the composition of the mass ejected by each stellar population. Using OMEGA+ provides two main advantages compared to using OMEGA alone: the star formation rate can be self-calculated from the balance between galactic inflows and stellar feedback, and the metals ejected outside the galaxy are mixed with the CGM reservoir and can be recycled into the star-forming region via galactic inflows.

We next present the set of equations that drive the evolution of our galaxy model, which represents one branch of the merger tree. Since we plan to calibrate our model for the high redshift universe, some of our parametrizations are exploratory.

4.2.1. Initial Conditions

Each galaxy is embedded in a virialized system defined by

$$V_{\text{vir}}^2 = \frac{GM_{\text{vir}}}{R_{\text{vir}}}, \quad (2)$$

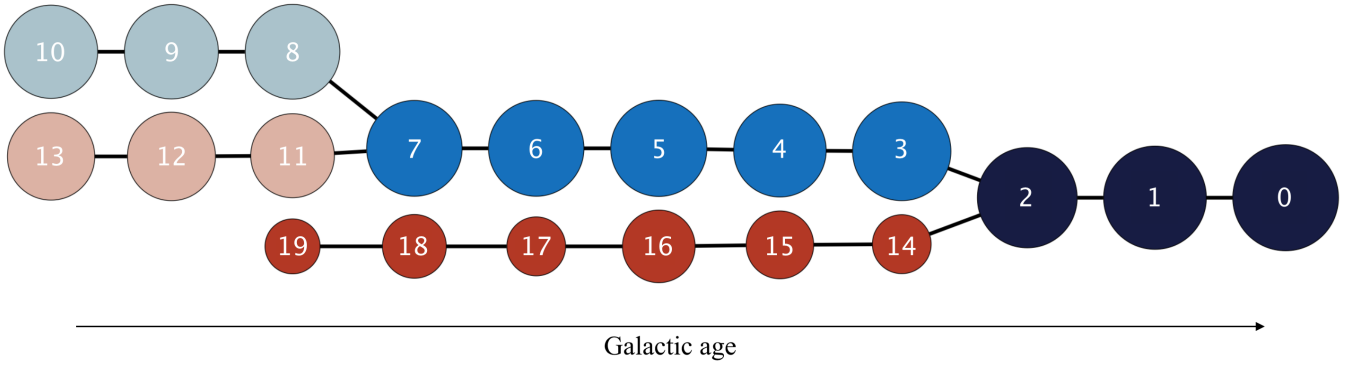


Figure 6. Illustration of the terminology used in this work. Each circle represents a halo at a particular snapshot, a tree-node in the merger tree, where the radius of that circle scales with $\log M_{\text{vir}}$. Tree-nodes connected together by the same color are defined as a “branch,” and refer to an isolated building-block galaxy. These individual galaxies are simulated with **OMEGA+** (Section 4.2) while their interaction with each other and the hierarchical assembly of the target galaxy is orchestrated by **GAMMA** (Section 4.1). The number listed on each tree-node refers to its depth-first order when sorting the merger tree (see also Figure 1 in Riebe et al. 2013). In this case, the most massive progenitors correspond to the tree-node segment labelled from 0 to 10.

where G is the gravitational constant and V_{vir} , M_{vir} , and R_{vir} are the virial velocity, mass, and radius, respectively (see Section 3.3). M_{vir} , which includes the dark matter and baryonic mass, and R_{vir} are provided by **GAMMA** as input parameters. The virial temperature T_{vir} of the system is defined by (Barkana & Loeb 2001)

$$k_{\text{B}}T_{\text{vir}} = \frac{1}{2}\mu m_{\text{H}}V_{\text{vir}}^2 \quad (3)$$

and is assumed to be the temperature of the CGM gas filling the dark matter halo (White & Frenk 1991). In this last equation, k_{B} is the Boltzmann constant, μ the mean molecular weight (which can range from 0.6 to 1.2), and m_{H} the mass of a hydrogen atom. T_{vir} is usually used to calculate the cooling timescale of the CGM. However, for the high-redshift galaxy considered in this work, this timescale is too short to be used in the gas circulation process (see Section 4.2.4).

A *primordial* galaxy within the context of this paper refers to a galaxy that is not the result of a galaxy merger, but rather forms directly out of virializing dark matter particles or sub-resolution dark matter halos. In that case, the gas fraction of the system is set to the universal baryonic fraction and all the of gas is deposited in the CGM, assuming a primordial composition,

$$M_{\text{CGM}}(t=0) = \frac{\Omega_{b,0}}{\Omega_0} M_{\text{vir}}. \quad (4)$$

As in the W12 simulation, the cosmological parameters adopted in this work come from Komatsu et al. (2011), with the relevant parameters being $\Omega_{b,0} = 0.0449$, $\Omega_{\Lambda} = 0.734$, and $h = 0.71$. In Equation (4), $t = 0$ refers to the formation time of the considered galaxy (or branch), and not the beginning of the cosmological simulation. The

actual simulation time is traced by **GAMMA** in order to orchestrate the formation of the different building-block galaxies.

If a galaxy is not primordial but is the result of a merger, **OMEGA+** then uses the input conditions provided by **GAMMA** regarding existing stellar populations and the mass and composition of the gas components. Such initial conditions are obtained by summing the components of each progenitor system (i.e., all galactic gas components are combined together).

4.2.2. Overall Gas Circulation

Here we present the main equations describing the mass exchange between the different components of **OMEGA+**. The time evolution of M_{gas} , the mass of the cold gas reservoir (galactic gas), is defined by the following differential equation,

$$\dot{M}_{\text{gas}} = \dot{M}_{\text{g,in}} + \dot{M}_{\text{ej}} - \dot{M}_{\star} - \dot{M}_{\text{g,out}}, \quad (5)$$

where the four terms on the right-hand side are the inflow rate from the CGM into the galaxy ($\dot{M}_{\text{g,in}}$), the combined mass-loss rate of all stars (\dot{M}_{ej}), the star formation rate (\dot{M}_{\star}), and the outflow rate from the galaxy into the CGM ($\dot{M}_{\text{g,out}}$). While the magnitude of the star formation rate drives how much metal mass is ejected by stars, the galactic inflows typically dilute the metallicity of the galactic gas (Finlator 2017). We refer to Davé et al. (2012) for an analytical model where all the physical processes stated above are in equilibrium. The time evolution of M_{CGM} , the mass of the hot gas reservoir (CGM), is defined by

$$\dot{M}_{\text{CGM}} = \dot{M}_{\text{CGM,in}} + \dot{M}_{\text{g,out}} - \dot{M}_{\text{g,in}} - \dot{M}_{\text{CGM,out}}, \quad (6)$$

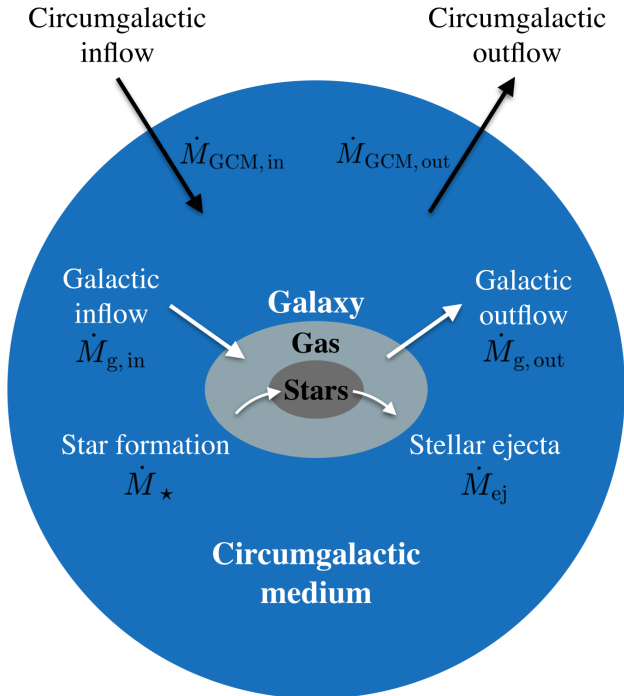


Figure 7. Structure overview of **OMEGA+**. The cold star-forming gas (the galaxy) is located at the center of a hot gas reservoir (the circumgalactic medium) filling the host dark matter halo. The arrows show the different mass transfer processes between the different gas components, as described in Section 4.2. Within this framework, the region outside the circumgalactic medium is called the external medium. **GAMMA**, defined in Section 4.1, uses **OMEGA+** on top of each branch of the merger tree.

where $\dot{M}_{\text{CGM,in}}$ is the inflow rate from the external medium into the CGM, and $\dot{M}_{\text{CGM,out}}$ is the outflow rate from the CGM into the external medium. All terms presented in Equations (5) and (6) evolve as a function of time and are described in more details below (see also Figure 7).

4.2.3. Circumgalactic Inflows

The CGM can increase its mass by accreting gas from the external medium. Since we do not follow the evolution of this external gas reservoir with **GAMMA**, the mass gained by the CGM during a timestep is based on how much dark matter has been accreted. Assuming a universal baryonic fraction, the mass accretion rate from the external medium to the CGM is defined by

$$\dot{M}_{\text{CGM,in}} = \dot{M}_{\text{DM}} \left(\frac{\Omega_{\text{M},0}}{\Omega_{\text{b},0}} - 1 \right)^{-1}, \quad (7)$$

where the growth rate of the dark matter mass \dot{M}_{DM} is extracted from the merger tree and provided by **GAMMA**. The mass accreted is assumed to have a primordial com-

position. Note that this is not entirely representative of the hydrodynamic simulation, as metals ejected outside the virial radius can be re-accreted at a later time and metals ejected by surrounding galaxies can be introduced in the halo of the considered galaxy (see also [Anglés-Alcázar et al. 2017](#)).

If the dark matter mass decreases during a timestep, we calculate the fraction of dark matter lost and use that fraction to remove gas from the CGM in the same proportion. We do not use Equation (7) in this case because the gas fraction in the CGM does not always reflect the universal baryonic ratio ($\Omega_{\text{b},0}/\Omega_{\text{M},0}$). Indeed, CGM outflows can reduce the gas fraction by expelling gas beyond the virial radius (see Section 4.2.7).

4.2.4. Galactic Inflows

The rate at which the CGM gas is introduced inside the galactic gas is defined by

$$\dot{M}_{\text{g,in}} = \frac{M_{\text{CGM}}}{\tau_{\text{inflow}}}, \quad (8)$$

where τ_{inflow} represents the inflow timescale. We refer to [Lu et al. \(2011\)](#) for more details on the inflow prescriptions typically used in semi-analytic models. The time needed for the hot gas to be transferred in the central galaxy depends on how fast gas can cool (cooling timescale, τ_{cool}) and how fast gas can physically travel from the CGM to the galaxy (free-fall timescale, τ_{ff}). Those timescales are defined as ([White & Frenk 1991](#))

$$\tau_{\text{cool}} = \frac{3k_{\text{B}}T}{2n_{\text{e}}\Lambda(T, Z)}, \quad (9)$$

$$\tau_{\text{ff}} = 0.1H_0^{-1}(1+z)^{-3/2}, \quad (10)$$

where n_{e} and H_0 are the electron number density and the current Hubble parameter, respectively. The cooling function Λ depends on the temperature T and metallicity Z of the gas reservoir, here the CGM. Equation (10) actually refers to 10% the Hubble time in an Einstein-de Sitter universe, which is a reasonable approximation for the dynamical timescale of a halo. In our model, however, this equation is only used to provide a default setup for the redshift-dependent gas inflow timescale, which is modified by exploratory parameters as described below.

We used **Grackle**⁵ ([Smith et al. 2017](#)) to calculate the average cooling timescale of the CGM, assuming it is heated to T_{vir} . For halos forming the bulk of the final stellar mass in the W12 simulation, we found that τ_{cool} is always shorter than τ_{ff} because of the high gas density at high redshift. For the purpose of this paper, we therefore

⁵ <http://grackle.readthedocs.io/en/grackle-3.0/>

do not use τ_{cool} to calculate the inflow timescale and do not need to track the density and temperature of the CGM. We define the inflow timescale of cooling gas as

$$\tau_{\text{inflow}} = 0.1H_0^{-1}C_\tau(1+z)^{-3\gamma_{\text{ff}}/2}, \quad (11)$$

$$C_\tau = 10H_0\tau_{\text{inflow},0}(1+z_f)^{3\gamma_{\text{ff}}/2}, \quad (12)$$

where $\tau_{\text{inflow},0}$ is the gas inflow timescale of the final galaxy (the resulting most massive branch in the merger tree) at the end of the simulation at redshift z_f . When using **GAMMA**, the value of $\tau_{\text{inflow},0}$ is the same for all **OMEGA+** instances, so that each building-block galaxies considered in the merger tree evolves following the same set of equations. The γ_{ff} parameter has been introduced to explore different redshift dependencies, with the goal to provide maximum flexibility to compare our SAM with hydrodynamic simulations. When $\gamma_{\text{ff}} = 1$, the gas inflow timescale scales linearly with the free-fall timescale. The impact of $\tau_{\text{inflow},0}$ and γ_{ff} on the temporal evolution of τ_{inflow} and on the predicted SFH and MDF is presented in Section 5.2 and shown in the second row of Figure 8.

4.2.5. Star Formation

The star formation in **OMEGA+** depends linearly on the mass of the cold gas reservoir (e.g., [Springel et al. 2001](#); [Baugh 2006](#)):

$$\dot{M}_\star = \frac{\epsilon_\star}{\tau_\star}M_{\text{gas}} = f_\star M_{\text{gas}}, \quad (13)$$

where ϵ_\star is the dimensionless star formation efficiency (SFE) and τ_\star is the star formation timescale. We combine these two last parameter into a single SFE parameter (f_\star) which has units of yr^{-1} . Here we allow f_\star to vary as a function of the dark matter halo mass of the galaxy and define the SFE as

$$f_\star = f_{\star,0} \left(\frac{M_{\text{DM}}}{M_{\text{DM},0}} \right)^{\gamma_\star}, \quad (14)$$

where $f_{\star,0}$ and $M_{\text{DM},0}$ are the SFE and dark matter mass of the final galaxy at the end of the simulation. The former is a free parameter while the latter given by **GAMMA**. The γ_\star parameter controls the power-law dependence of the star formation efficiency on the size of the dark matter halo, M_{DM} , and should be considered to be an exploratory parameter. As for γ_{ff} (see Section 4.2.4), the value of γ_\star is the same for all **OMEGA+** instances when using **GAMMA**. The impact of $f_{\star,0}$ and γ_\star on the temporal evolution of f_\star and on the predicted SFH and MDF is presented in Section 5.1 and shown in the first row of Figure 8.

4.2.6. Galactic Outflows

In our model, galactic outflows (the mass ejected from the galaxy into the CGM) are driven by the mechanical energy released by massive stars. The outflow rate is therefore based on the mass-loading factor defined by [Murray et al. \(2005\)](#):

$$\eta_{\text{gal}} = \frac{\dot{M}_{\text{g,out}}}{M_\star}. \quad (15)$$

According to [Murray et al. \(2005\)](#),

$$\eta_{\text{gal}} \propto v_{\text{out}}^{-\gamma_\eta}, \quad (16)$$

where v_{out} is the velocity of the gas contained in the outflow. In [Murray et al. \(2005\)](#), $\gamma_\eta = 1$ for momentum-driven outflows and $\gamma_\eta = 2$ for energy-driven outflows. We note that γ_η can be larger than 2 for low-mass dwarf galaxies ([Muratov et al. 2015](#)). [Martin \(2005\)](#) found that the outflow velocity of galaxies correlates with their rotation velocities, which related to the velocity V_{vir} of the virialized systems (see [Somerville & Davé 2015](#)). By replacing v_{out} by V_{vir} in Equation (16), and by substituting V_{vir} with Equation (2), the mass-loading factor becomes dependent on M_{vir} and R_{vir} . Using the relation between R_{vir} , M_{vir} , and redshift z found in [White & Frenk \(1991\)](#), the mass-loading factor can be expressed as follow (see derivation in [Côté et al. 2017a](#))

$$\eta_{\text{gal}} = C_\eta M_{\text{DM}}^{-\gamma_\eta/3} (1+z)^{-\gamma_\eta/2}, \quad (17)$$

$$C_\eta = \eta_{\text{gal},0} M_{\text{DM},0}^{\gamma_\eta/3} (1+z_f)^{\gamma_\eta/2}, \quad (18)$$

where $\eta_{\text{gal},0}$ is a free parameter representing the mass-loading factor of the final galaxy at the end the simulation.

As with γ_{ff} (see Section 4.2.4), γ_η is also set as a free parameter for which its value is the same for all **OMEGA+** instances. We refer to [Bustard et al. \(2016\)](#) for alternative approaches to model galactic outflows. The impact of $\eta_{\text{gal},0}$ and γ_η on the temporal evolution of η_{gal} and on the predicted SFH and MDF is presented in Section 5.3 and shown in the third row of Figure 8. In this work, Equations (17) and (18) and their free parameters represent an exploratory parametrization to allow flexibility to reproduce the high-redshift hydrodynamic simulation. In future work we plan to use the latter simulation to derive analytical prescriptions to be used in SAMs, as done in [Hopkins et al. \(2012\)](#) and [Muratov et al. \(2015\)](#).

At a given time t_i , associated with the i^{th} timestep, the mass of the galactic outflow driven by the i^{th} SSP is defined by

$$M_{\text{g,out}}^i = \eta_{\text{gal}}(t_i) \dot{M}_\star(t_i) \Delta t_i, \quad (19)$$

where Δt_i is the duration of the i^{th} timestep⁶. This outflowing mass is then distributed in time following the evolution of the mechanical luminosity $L_*(t)$ released by the stars of the i^{th} SSP. In **OMEGA+**, $L_*(t)$ is re-normalized such that

$$\int_0^\infty L_*(t) dt = 1. \quad (20)$$

Integrating $L_*(t)$ over a certain time interval thus represents the fraction of the total outflowing mass (see Equation 19) lost at each timestep. In our code, $L_*(t)$ can be of any form. However, in this paper, we use a constant luminosity from 4 to 20 Myr in order to be consistent with the SNe feedback implemented in **Wise et al. (2012a)**. Below 4 Myr and above 20 Myr, $L_*(t)$ is set to zero.

At any time t , the total mass ejected from the galaxy over a time Δt is obtained by summing the contribution of all SSPs,

$$M_{\text{g,out}}(t) = \sum_i^{N_{\text{SSP}}} M_{\text{g,out}}^i \int_{t-t_i}^{t-t_i+\Delta t} L_*(t) dt. \quad (21)$$

In this last equation, $t - t_i$ represents the age of the i^{th} SSP. The summation assumes a cumulative process in the sense that twice as much energy will lead to twice as much outflowing gas. In other words, no nonlinear interaction is assumed between the different SSPs that contribute to an outflow.

4.2.7. Circumgalactic Outflows

The mass introduced into the CGM by galactic outflows can generate an excess of energy. When this happens, a fraction of the hot gas contained in the CGM can be expelled outside the host dark matter halo (e.g., **Croton et al. 2006**). Because this feedback process is driven by galactic outflows, which are driven by stellar feedback, we use the mass-loading factor definition to describe the CGM outflow rate, as in equation (15),

$$\eta_{\text{CGM}} = \frac{\dot{M}_{\text{CGM,out}}}{\dot{M}_*}. \quad (22)$$

We then assume that the CGM outflow rate is proportional to the galactic outflow rate through the free parameter f_η . The CGM outflow rate is then given by

$$\dot{M}_{\text{CGM,out}} = f_\eta \eta_{\text{gal}} \dot{M}_*. \quad (23)$$

⁶ As for **SYGMA** and **OMEGA**, the timesteps in **OMEGA+** and **GAMMA** can vary arbitrarily as a function of time. See https://github.com/NuGrid/NuPyCEE/blob/master/DOC/Capabilities/Timesteps_size_management.ipynb

In the current version of **OMEGA+**, when a CGM outflow is generated, the mass lost is not kept in a separate reservoir to be reincorporated later on in the virialized system – rather, it is assumed that the cooling time of this gas is long enough that it is greater than the current Hubble time in the model, and thus will not return to the halo on a time scale that is relevant to the calculation. The impact of f_η on the predicted SFH and MDF is presented in Section 5.4 and shown in the last row of Figure 8.

4.3. Stellar Yields

Because of their connection with the JINA-NuGrid chemical evolution pipeline (**Côté et al. 2017b**), **OMEGA+** and **GAMMA** automatically have access to the complete NuPyCEE⁷ stellar yields library. In practice, a simulation with **GAMMA** can include as many elements as desired, including the 280 isotopes available with NuGrid yields (**Pignatari et al. 2016; Ritter et al. 2017**). In addition, an arbitrary number of enrichment sources can be included such as compact binary mergers, Type Ia supernovae, neutrino-driven winds in core-collapse SNe, and any other sources that can be modelled using a set of yields and a delay-time distribution function⁸.

However, in this work, because we want to be consistent with the W12 simulation, we do not follow individual species – we only follow the total mass of metals. Throughout this paper, each SSP will eject 25% of its original mass via SNe. As in W12, the metallicity in mass fraction of all stellar ejecta is $Z = 0.02$.

5. IMPACT OF INPUT PARAMETERS

In this section we combine **GAMMA** with the merger tree of the most massive galaxy found in the W12 calculation and compare its predictions with the equivalent quantities extracted from the hydrodynamic simulations. The goal of this section is to show variations of the model parameters impact our predictions, rather than tuning **GAMMA** to best match the results obtained by the W12 calculation (which is shown in Section 7). In the following subsections we discuss Figure 8, which focuses on variations in fundamental physical quantities such as the star formation efficiency and the gas inflow timescale rather than on specific input parameters. This is because different parameterizations can be used in different studies, while fundamental processes such as star formation and gas circulation are inherent to most chemical evolution and semi-analytic models. The input parame-

⁷ <http://github.com/NuGrid/NuPyCEE>

⁸ https://github.com/NuGrid/NuPyCEE/blob/master/DOC/Capabilities/Delayed_extra_sources.ipynb

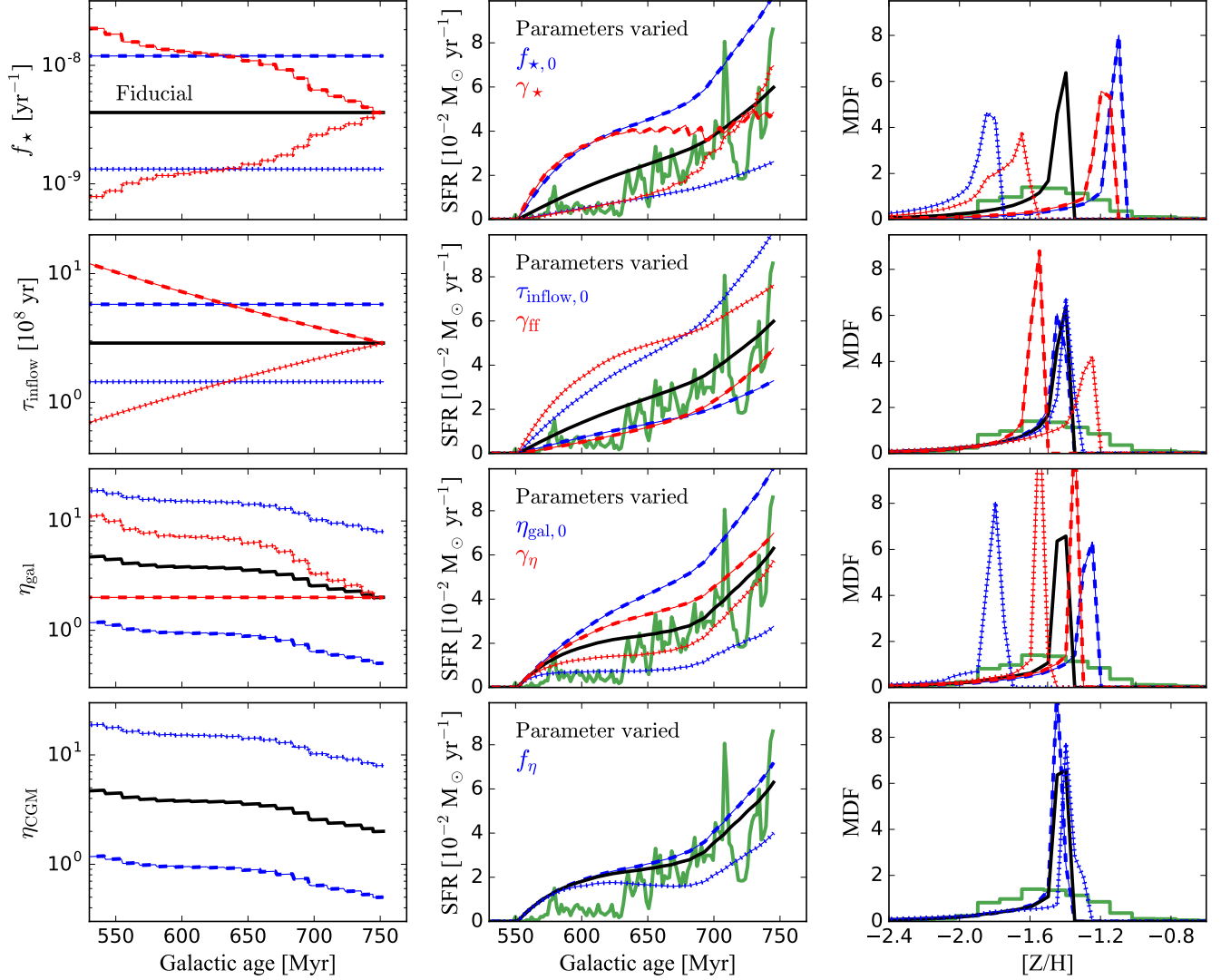


Figure 8. Impact of our input parameters (left column) on the predicted star formation history (middle column) and metallicity distribution function (right column) using GAMMA with the target galaxy’s merger tree. The green lines in the middle and right columns display the physical values extracted from the hydrodynamic simulation. In each row, only one key physical quantity has been modified (left panel), and the different line styles are used to keep track of each case. The fiducial case is shown as the black solid line. The physical quantities shown in the three first top rows are controlled by two parameters, and their individual impact is highlighted using different colors (see Table 1). **Top row:** Star formation efficiency (f_* , Equation 14). Variation of $f_{*,0}$ is shown by the blue lines, and γ_* by the red lines. **Second row:** Gas inflow timescale (τ_{inflow} , Equation 12) used to calculate the rate at which the hot gas reservoir (CGM) is introduced in the star-forming region. Variation of $\tau_{\text{inflow},0}$ is represented by the blue lines, and γ_{ff} by the red lines. **Third row:** Mass-loading factor of the galaxy (η_{gal} , Equation 18) representing the mass transfer of gas from the star-forming region to the hot gas reservoir. Variation of $\eta_{\text{gal},0}$ is shown by the blue lines, and γ_{η} by the red lines. **Bottom row:** Mass-loading factor of the hot gas reservoir (η_{CGM} , Equation 23) representing the mass transfer of gas from the hot gas reservoir to the external medium (outside the virial radius). We note that none of the metallicity distribution functions produced in this parameter exploration match the broad distribution extracted from the simulations. We explain the reason for this disagreement in Section 6.

ters used in this section to control those physical quantities are summarized in Table 1.

When interpreting the following subsections, it is important to note that the predictions shown in the top two and bottom two rows of Figure 8 assumed different fiducial values for the parameters (these are also indicated in Table 1). This is motivated by two reasons. First, to facilitate the building of intuition, since the impact of different parameters are best visualized in different *galaxy evolution regimes*. And second, we want to highlight that, under certain circumstances, different physical quantities can in principle modify the predicted SFR and MDF in a similar way.

To show the impact of the star formation efficiency (SFE), we adopt weak galactic outflows to minimize their impact on the predictions. Otherwise, when increasing the SFE and reducing the mass of galactic gas, outflows would start to significantly alter the star formation history by generating episodic behaviours, which are less trivial to interpret in the context of this section (but see Section 7.1 and Figure 11). With stronger outflows, previous studies shown that the SFE has little impact on the SFR of galaxies due to a balance between star formation and feedback (e.g., Schaye et al. 2010; Hopkins et al. 2011; Lagos et al. 2011). Our target galaxy, however, only efficiently formed stars for ~ 200 Myr and did not reach an equilibrium state by the end of the simulation. The large variations shown in this section caused by the SFE should not be taken as a general case. To show the impact of galactic and CGM outflows (bottom two rows of Figure 8), they need to be strong. Otherwise, if they are too weak relative to the amount of gas available, not enough gas would be removed from the galaxy and the CGM to significantly alter the star formation history and the metallicity distribution function.

Some quantities seen in Figure 8 show discrete steps in their temporal profiles. This is because in the most massive galaxy found in the simulation, there is typically at least one merger with a non-star-forming halo between data outputs. This means we do not always have access to the time-evolution of the properties of halos (e.g., M_{vir}) within a branch of the merger tree. When this occurs, we input constant halo properties in OMEGA+, which in turn fixes parameters that depend on M_{vir} (e.g., f_{\star} , η_{gal}) to a constant value.

5.1. Star Formation Efficiency

The top row of Figure 8 shows the impact of the star formation efficiency (SFE; f_{\star}) adopted in GAMMA (left panel) on the predicted star formation history (SFH; middle panel) and metallicity distribution func-

tion (MDF; right panel). The magnitude of the SFE is controlled by the $f_{\star,0}$ parameter (Equation 14). A higher SFE generates higher SFRs and increases the total stellar mass formed by the end of the simulation (see blue lines). Overall, the shape of the temporal profile of the SFH stays similar when the SFE is scaled up and down by a constant factor. The main role of the SFE in a chemical evolution code is to modify the stellar-to-gas mass ratio in the galactic component. By increasing the SFE, the metals ejected by stars are thus deposited in greater concentration relative to the mass of gas and the peak of the MDF is pushed to higher metallicities, and vice-versa.

The shape of the SFH is affected by the shape of the temporal profile of the SFE (see red lines). The time-dependence of this latter quantity originates from its relation with the dark matter halo mass of the host galaxy. This relation is controlled by the γ_{\star} parameter in the form of a power law (Equation 14). A SFE that decreases with time tends to form more stars at early time and less stars at later time compared to a constant SFE. In our case, this generates an initial star formation burst followed by a relatively flat SFR (red dashed line). On the other hand, a SFE that increases with time tends to generate an ever-increasing SFR (red dotted line) since gas gets increasingly efficient in turning into stars.

5.2. Inflow Timescale

The second row of Figure 8 shows the impact of the inflow timescale τ_{inflow} , which sets the gas transfer rate from the CGM into the galactic component (Equation 8). The magnitude of the timescale is set by the $\tau_{\text{inflow},0}$ parameter, while the slope of its temporal profile is controlled by γ_{ff} (Equation 12). A lower τ_{inflow} increases the SFR of the galaxy because the CGM gas is introduced more rapidly in the galactic component to fuel the star formation (see blue lines), and vice-versa. The MDF is similar from one run to another because the shape of the inflow timescale and the SFE value were kept unchanged. Although the total mass of stars and gas scale with τ_{inflow} , the stellar-to-gas mass ratio and thus the metal concentration remain the same (see Section 5.1).

As for the SFE, modifying the slope of the inflow timescale modifies the shape of the SFH (red lines). Adopting an increasing trend as a function of time for τ_{inflow} will tend to form more stars at early times and less stars at later times in comparison to a constant τ_{inflow} , and vice-versa. The MDF is also affected by the shape of τ_{inflow} , since it modifies the final mass of gas present in the galactic component at the end of the simulation. For example, for two galaxies that will form in total the

Table 1. Input parameters used in **GAMMA** to produce Figure 8.

Parameter	Description	Values in top	Values in bottom	Modified in row (from top to bottom)
		rows (f_* , τ_{inflow})	rows (η_{gal} , η_{CGM})	
$f_{*,0}$	Final SFE value at z_f [10^{-9} yr^{-1}]	(1.3, 4.0 , 12.0)	6.0	1 (f_* , Equation 14)
γ_*	DM mass dependency for the SFE	(−1.0, 0.0 , 1.0)	0.0	
$\tau_{\text{inflow},0}$	Final inflow timescale at z_f [$\tau_{\text{ff},0}$]	(2.5, 5.0 , 10.0)	3.5	2 (τ_{inflow} , Equation 12)
γ_{ff}	Redshift dependency for the inflow timescale	(−4.0, 0.0 , 4.0)	0	
$\eta_{\text{gal},0}$	Final galactic mass-loading factor at z_f	1.0	(0.5, 2.0 , 8.0)	3 (η_{gal} , Equation 18)
γ_η	Galactic mass-loading power-law index	0.0	(0.0, 2.0 , 4.0)	
f_η	CGM mass-loading factor scaling [η_{gal}]	0.0	(0.25, 1.0 , 4.0)	4 (η_{CGM} , Equation 23)

NOTE—We used different sets of input parameter values for the top and bottom panels of Figure 8 to better highlight the impact of each parameter. The fiducial values are shown in boldface while the ones used when a parameter is varied are shown in parenthesis. SFE stands for star formation efficiency, DM for dark matter, z_f for final redshift, and CGM for circumgalactic medium.

same amount of stars (blue and red dashed lines), the galaxy with a decreasing τ_{inflow} will have to form more stars at later time compared to the one with a constant τ_{inflow} , in order to compensate for the lower SFR at early time. This late star formation enhancement requires a large amount of inflowing gas. As a result, the galaxy with a decreasing τ_{inflow} as a function of time will end up with more gas in the galactic component compared to the galaxy with a constant τ_{inflow} , which dilutes the metallicity and pushes the peak of the MDF to lower metallicities.

5.3. Galactic Mass-Loading Factor

The third row of Figure 8 shows the impact of the galactic mass-loading factor, η_{gal} , which sets the mass transfer from the galaxy to the CGM via galactic outflows (Equation 15). This quantity scales with $\eta_{\text{gal},0}$ while its temporal profile is defined by γ_η (Equation 18). When η_{gal} is increased by a constant factor, the SFR is reduced because more gas is ejected from the galaxy (blue lines). Recall that the star formation history is self-generated with **OMEGA+**. With **OMEGA**, the SFH is an input parameter and galactic outflows are balanced by galactic inflows in order to sustain the desired SFH (Côté et al. 2017a). With **OMEGA+**, inflows and outflows are not directly connected and the SFH can thus be modified by η_{gal} .

Galactic outflows are efficient mechanisms to remove metals from galaxies. A stronger outflow will systematically shift the peak of the MDF to lower metallicities, and vice-versa (see also Andrews et al. 2017). Modifying the shape of η_{gal} affects the shape of the SFH because

it changes the way the mass of gas inside the galaxy is evolving with time.

5.4. Circumgalactic Mass-Loading Factor

The bottom row of Figure 8 shows the impact of the CGM mass-loading factor, η_{CGM} , which sets the gas transfer rate from the CGM to the external medium (which one could think of as the truly intergalactic medium). It is directly related to η_{gal} via the proportionality constant f_η (Equation 23). Because the galactic inflow rate depends on the mass of the CGM (Equation 8), the strength of a CGM outflow regulates the mass of the galactic gas and thus the star formation history. In Figure 8, the SFH eventually saturates when η_{CGM} is decreased (blue dashed line) since the CGM outflow rate becomes negligible relative to the total mass of the CGM.

In terms of the scaling of the inflow timescale, changing the CGM outflow rate by a constant factor does not significantly shift the peak value of the MDF. This is because the stellar-to-gas mass ratio in the galactic component does not depend on the amount of inflowing gas, as long as the temporal profile (not the magnitude) of the inflows and star formation efficiency are kept unchanged (see Section 5.2).

6. NON-UNIFORM MIXING OF METALS

As seen in Figure 8, no combinations of input parameters can generate a MDF with **GAMMA** that is as broad as is seen in the hydrodynamic simulation. This is because each building-block galaxy in **GAMMA** is represented by a uniformly-mixed one-zone model (**OMEGA**). This implies

that the star-forming gas has only one metallicity value per timestep, which can be seen as the mass-weighted mean metallicity of what should be a non-uniformly-mixed medium. In **GAMMA**, all stars formed during a timestep in a given branch therefore have the same initial metallicity, as opposed to in hydrodynamic simulations that show star formation in a range of metallicities at a given point in time in the target galaxy and its largest satellite. Uniformly-mixed models tend to create a narrow MDF with a sharp break at its high-metallicity end when a galaxy is in an active accretion phase (Weinberg et al. 2017), which is the case here.

Figure 3 shows that the dispersion of metallicity in the W12 simulation is stochastic and depends on time and on the characteristics of the particular progenitor galaxy. If we ignore the largest dispersions caused by triggered star formation, as shown in Section 3.5 (a reasonable approximation, because very little stellar mass is produced in these events), the dispersion in the main galaxy increases as a function of time (green dots) while it decreases in the smaller satellite galaxy (pink dots). We recall that the MDFs of metal-poor stars observed today in real galaxies represent the combination of several low-mass galaxies that likely had different enrichment histories.

The histograms in Figure 9 show the stellar metallicity distributions taken at different times, as indicated on the figure, for the main galaxy. Some distributions can be represented by Gaussian functions with different standard deviations (upper panel). This justifies the process of convolving the MDF with a Gaussian function in order to reproduce observations with simple models (e.g., Fenner & Gibson 2003; Pilkington & Gibson 2012; Vincenzo et al. 2016; Côté et al. 2016b). However, at earlier times, the metallicity distributions have more complex shapes that are not well reproduced by individual Gaussians (middle panel). This deviation from a Gaussian distribution could, however, be caused by insufficient sampling due to the low number of stellar populations formed. When triggered star formation events occur, the contribution of distinct stellar populations can be seen in the metallicity dispersion profile (bottom panel).

To induce spread in the MDF predicted by **GAMMA**, we post-process our results by convolving the MDF of all building-block galaxies by a Gaussian function with a standard deviation of 0.2, a value extracted from the hydrodynamic simulation at late times. As seen in Figure 10, this convolution process significantly improves the agreement between the semi-analytic and hydrodynamic approaches at the final redshift. Although more cases need to be investigated before deriving a general

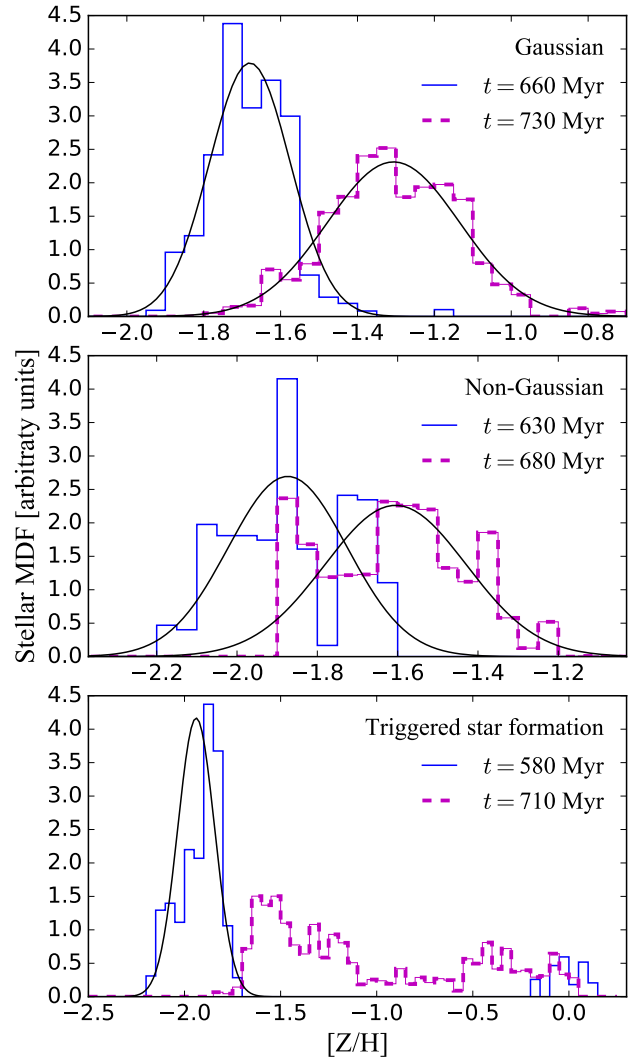


Figure 9. Examples of metallicity distribution functions (histograms) of all stars formed during a certain time interval in the target galaxy. The middle value of the time intervals, which has a range of 10 Myr in all cases, is labelled in each panel. The solid black curves represent Gaussian fits. There is no **GAMMA** prediction in this figure. **Top panel:** Distributions that are well described by a Gaussian function. **Middle panel:** Distributions that are not well described by a Gaussian function. This could be due, however, to insufficient sampling. **Bottom panel:** Distributions that include a triggered star-formation process suddenly generating high-metallicity stars compared to the average gas metallicity (see Figure 3).

prescription for SAMs, our results suggests that non-uniform mixing can be captured by simple models in a post-processing manner. However, when modeling the chemical evolution of different elements, the situation becomes more complex because different abundance ratios detected in metal-poor stars have different dispersions depending on the targeted elements (e.g., Cohen

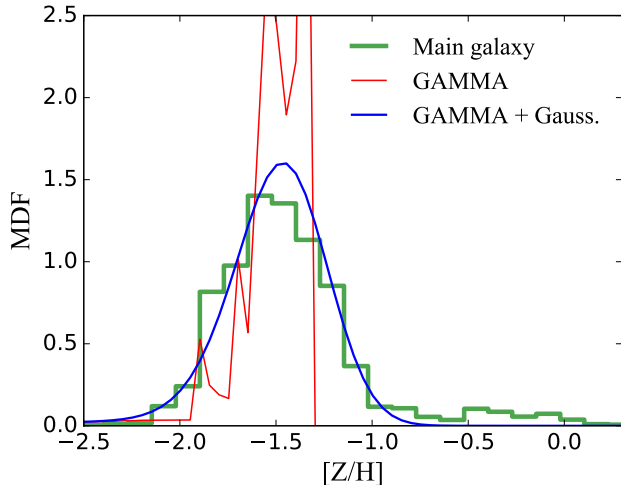


Figure 10. Metallicity distribution function (MDF) predicted by **GAMMA** compared to the one extracted from the hydrodynamic simulation (**W12**, green line) for the main galaxy. The red line represents the raw MDF while the blue line shows the result of convoluting this MDF with Gaussian functions having a standard deviation of 0.2 (see Section 6). The long high-metallicity tail seen in the **W12** simulation originates from triggered star-formation events (see Figure 3). The **GAMMA** model presented in this figure corresponds to the blue model in Figure 11 (see Section 7).

et al. 2013; Roederer et al. 2014; Frebel & Norris 2015; Hirai et al. 2017). Deriving analytic prescriptions for the non-uniform mixing of individual elements is not possible with the **W12** simulation, since only the overall metallicity was tracked rather than individual species abundances.

In spite of our ability to reproduce the MDF of the hydrodynamic simulation at the final redshift, we cannot capture the triggered star formation events predicted by this simulation. These stochastic events create the long high-metallicity tail in the MDF (see Figure 3), which is absent in the MDF predicted by **GAMMA** (see Figure 10).

7. REPRODUCING THE HYDRODYNAMIC SIMULATION

In this section we apply the non-uniform mixing prescription constructed in Section 6 and attempt to reproduce the *observable quantities* from the **W12** simulation that are presented in Section 3.5. The “best fit” models shown in this section have been found by tuning input parameters by hand. This is not a statistically rigorous approach, and is intended to be the first step of a long-term model calibration and optimization process that will be improved by using statistical tools such as Markov Chain Monte Carlo calculations, which are already part of our chemical evolution pipeline (see Côté et al. 2017b).

Figure 11 shows a comparison between the **W12** simulation and **GAMMA**, with panels *a-c* showing three particular parameterizations of f_* , τ_{inflow} , and η_{gal} that are quite dissimilar from each other (see also Table 2). However, all those parameterizations do a reasonable job of reproducing the observable properties of the target halo (panels *d-f*). We examine these in more detail in the following subsections.

7.1. Star Formation and Metallicity

Panels *d* and *e* of Figure 11 shows the star formation history and metallicity distribution functions predicted by **GAMMA** using three the different sets of input parameters presented in Table 2 (blue, red, and black lines). We cannot reproduce the bursty nature and the relatively small oscillation periods of the star formation history, but our three models are still able to reproduce the global trend of the hydrodynamic simulation (green thick line in each panel). The oscillating behaviour in the SFR our blue model prior ~ 700 Myr is discussed in Section 8.2. The MDFs predicted by our models are very similar to each other, although the adopted SFE and gas circulation processes are substantially different from one model to another (panels *a*, *b*, and *c*). This is because the input parameters can modify the MDF in a similar manner (see Section 5). It is therefore possible to vary those parameters in such a way that the impact of their variations is cancelled for these particular observables. This results is complementary to the work of Côté et al. 2017a who showed that only fitting the stellar abundance ratios of a real galaxy is insufficient to understand its evolution, since those observations can numerically be reproduced in multiple ways (i.e., there is significant degeneracy between these model parameters).

7.2. Age-Metallicity Relationship

Panel *f* of Figure 11 shows the age-metallicity relationship predicted by **GAMMA** for the main galaxy (thick lines) and for the satellite galaxy (thin lines) against the **W12** data (green and pink dots). Each line segment represents a building-block galaxy in the merger tree (or a branch). The segments tend to align and form continuous lines because most of the mergers are minor and involve low-mass halos that do not form stars. Although the merger tree of the main galaxy is complex (see Figure 5), this galaxy represents a relatively simple case because star formation predominantly occurs in the most massive progenitors at $z \lesssim 9$ (see Figure 2).

To match the satellite galaxy with each **GAMMA** model, we used the same input parameters as for the main galaxy (panels *a*, *b*, and *c* of Figure 11), but we scaled

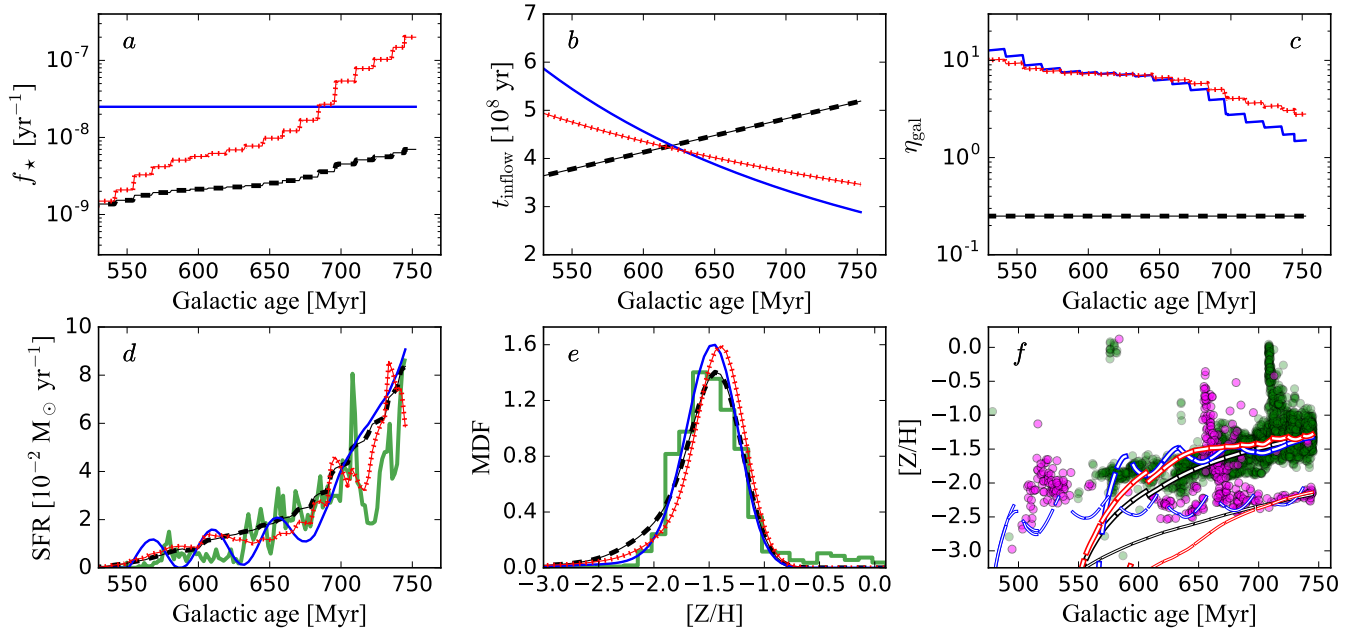


Figure 11. Comparison between the hydrodynamic simulation of Wise et al. (2012a) and the semi-analytic code **GAMMA** using the merger trees extracted from that simulation. **Top row:** The solid blue, dashed black, and red dotted lines represent three different **GAMMA** models using different assumptions for the evolution of the star formation efficiency (panel *a*), the gas inflow timescale (panel *b*), and the galactic mass-loading factor (panel *c*), as presented in Table 2. These three panels only show the predictions for the target galaxy, and do not explicitly target its satellite. **Bottom row:** Panels *d* and *e* show star formation history and metallicity distribution function (MDF) predicted by **GAMMA** compared to the ones predicted by the hydrodynamic simulation (green thick line), for the target galaxy. Panel *f* shows the age-metallicity relationship. For **GAMMA**, each color is associated to a specific model as in the other panels but the target and satellite galaxies are represented by thick and thin line segments (see Section 7.2), respectively. For the hydrodynamic simulation, the target and satellite galaxies are represented by green and pink dots, respectively.

down the magnitude of the star formation efficiency by a factor of 5. The slight differences seen in the low-metallicity end of the main galaxy’s MDFs predicted by our models (panel *e*) are more visible when looking at the age-metallicity relationship (panel *f*). Although the models are consistent with each others at late time ($t > 700$ Myr), they are divergent at earlier time. For the main galaxy, the black model best fits the W12 data between 650 and 700 Myr, while only the blue model is able reproduce the stellar metallicity at ~ 575 Myr. For the satellite galaxy, only the blue model can match the W12 data between 600 and 700 Myr. Its predictions at ~ 525 Myr are too low compared to W12, but the other models are at least an order of magnitude lower.

Overall, the blue model is our current best-fit model because of its fast early enrichment that allows to reproduce (although not perfectly) the age-metallicity relationship at all time, for both the main and the satellite galaxies. However, our predictions for the early stages of the age-metallicity relationship is likely affected by the current lack of pre-enrichment from Population III stars in **GAMMA**, which is present in W12 (see Section 8.2).

Table 2. Input parameters used for the three **GAMMA** models shown Figure 11.

Parameter	Model			Units
	Blue	Red	Black	
$f_{*,0}$	2.5	20.0	0.7	10^{-8} yr^{-1}
γ_*	0.0	3.0	1.0	–
$\tau_{\text{inflow},0}$	5.0	6.0	9.0	τ_{ff}
γ_{ff}	-2.0	-1.0	1.0	–
$\eta_{\text{gal},0}$	1.5	2.8	0.25	–
γ_{η}	5.0	3.0	0.0	–
f_{η}	0.0	0.0	0.0	η_{gal}

7.3. CGM Outflows

Figure 12 presents the total mass of gas and the total mass of metals found within the virial radius of the main galaxy as a function of time. As shown in Table 2, our best-fit **GAMMA** models do not include large-scale CGM

outflows ($f_\eta = 0.0$), meaning that all the gas is retained inside the virial radius. According to Figure 12, this assumption generates a good match with the quantity extracted from the hydrodynamic simulation (top thick green line) for the entire period of active star formation ($t \gtrsim 600$ Myr). This high baryonic retention, however, is likely to change if the simulation were to continue to lower redshifts ($z < 7$). Indeed, cosmological zoom-in simulations have shown that low-mass galaxies lose a significant fraction of their baryon by $z = 0$ (e.g., Muratov et al. 2015).

In Figure 12, variations can be seen between the simulation and the GAMMA models in between 400 and 600 Myr of galactic evolution. At 400 Myr, in the simulation, a Pop III explodes and triggers a short burst of star formation which generates a CGM outflow while the main galaxy is ~ 50 times less massive than at the end of the simulation. This event is not considered in our GAMMA models, which is why the total mass inside the halo in the simulation tends to be lower than our models during that period of time (see upper lines in Figure 12). The metal enrichment caused by this event can be seen as a bump in the mass of metals at ~ 420 Myr (bottom thick green line). After this time, the mass of metals decreases because mass is lost outside the virial radius. We note that the stellar mass formed during this event is negligible compared to the total mass formed during the active star formation period (see Figure 2).

Although a GCM outflow is generated at early time, the mass lost eventually falls back and returns into the galactic halo after ~ 600 Myr of evolution. This early starburst event provides a metallicity floor of $[Z/H] \sim -3$ at the onset of the active star formation period where our GAMMA models start to form stars (see discussion in Section 8.2). This could affect the metal-poor end of the MDF predicted by our models (see panel *e* of Figure 11). The slight increase in the mass of metals seen in the simulation at ~ 700 Myr compared to our model predictions is due to the infall of metal-rich gas accompanying the most massive satellite galaxy (see pink circle in Figure 4). We recall that since this satellite did not merge before the end of the simulation, it is not included in the merger tree of the main galaxy and its impact on the mass of metals is thus not accounted in the GAMMA models for the main galaxy.

8. DISCUSSION

In this section we discuss the limitations and uncertainties of this work, highlight the advantages of our approach, and describe the next steps required in this research to better constrain our semi-analytic model, GAMMA.

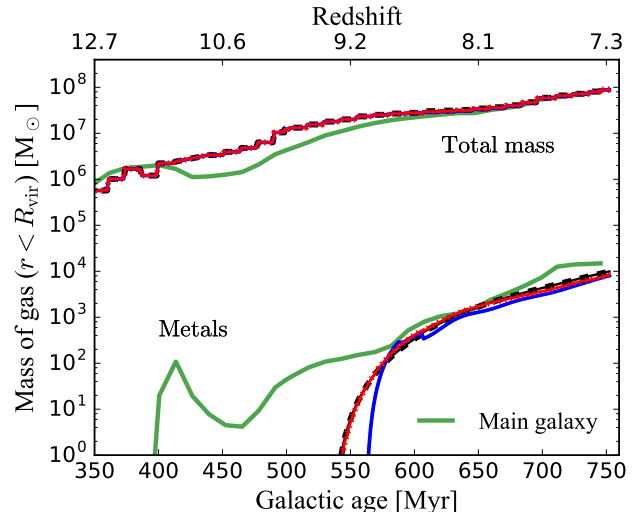


Figure 12. Total mass of gas (top lines) and mass of metals (bottom lines) present inside the virial radius of the main galaxy as a function of time. The thick green line represents the values extracted from the hydrodynamic simulation, while the solid blue, dashed black, and red dotted lines represent the three different GAMMA models presented in Figure 11.

8.1. Modeling Uncertainties

One of the most important sources of uncertainty in this project is the use of hydrodynamical simulations as “ground truth.” The W12 calculation is complex and includes a wide range of physics acting over a large span of spatial and temporal scales. A particular concern is the subgrid model for star formation and feedback used in this simulation – these subgrid models are, in general, the largest source of uncertainty in current-generation cosmological simulations of galaxy formation (see, e.g., Scannapieco et al. 2012; Naab & Ostriker 2017).

Figure 13 compares the stellar mass – halo mass relation from several “first galaxies” simulations (Pawlik et al. 2013; Xu et al. 2016; Kimm et al. 2017; Ma et al. 2017; Rosdahl et al. 2018). The galaxy studied in this work has a stellar mass nearly equal to the median found in the “Normal region” of the Renaissance simulations. In addition to the W12 and Renaissance Simulations, the simulations of Kimm et al. (2017) include Population III star formation. All simulations except Ma et al. (2017) solve the radiative transfer equation. At halo masses $M_{\text{vir}} \lesssim 10^8 M_\odot$, all of the simulation results are consistent with each other. Above this mass, the relation slope starts to increase in W12, the Renaissance Simulations, and Pawlik et al. (2013), whereas the SPHINX (Rosdahl et al. 2018) and FIRE-2 simulations (Ma et al. 2017) relation slope remains basically unchanged. The stellar masses from the SPHINX simulations are consis-

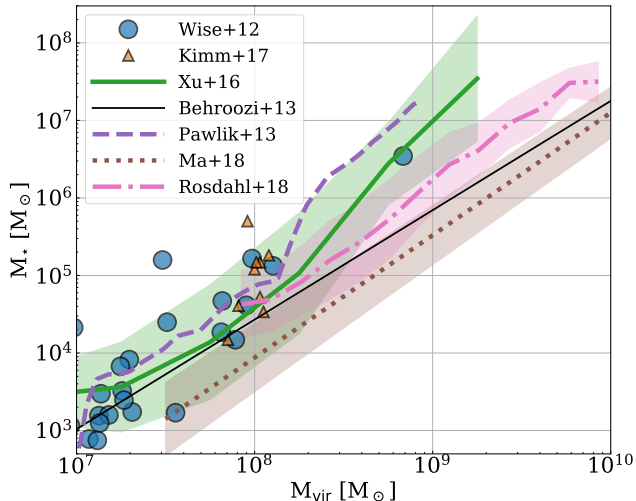


Figure 13. Comparison of the stellar mass growth as a function of halo mass between several simulations (see legend). The shaded areas depict $1\text{-}\sigma$ errors. The thin black line shows the abundance matching results at $z = 0$ extrapolated to low masses (Behroozi et al. 2013a). The stellar mass of the galaxy analyzed here is close to the median relation in the Renaissance Simulations (Xu et al. 2016), is consistent with the SPHINX simulations (Rosdahl et al. 2018), and is an order of magnitude higher than the FIRE-2 simulations (Ma et al. 2017).

tently a factor of 3–6 higher than the FIRE-2 simulations. The largest W12 galaxy is a factor of five higher than the median of the SPHINX simulations, however it should be noted that the Renaissance and SPHINX simulations’ stellar mass – halo mass relation are consistent to $1\text{-}\sigma$ over their overlapping halo mass range $10^8 - 10^{9.25} M_{\odot}$.

Furthermore, while the W12 calculation stops at a relatively low redshift that is observable by the Hubble Space Telescope ($z = 7.29$), even the most massive galaxy in this simulation is too dim to be seen by HST, even if strongly lensed. One important consequence of this is that the simulation we are using to validate and improve the GAMMA semi-analytical model is constrained by observations only indirectly, and thus will represent a significant source of uncertainty when GAMMA is ultimately used to make predictions about the relevant galaxy populations.

That said, there is significant utility in using the W12 simulation as a *case study*, to highlight possible missing or inaccurate physical prescriptions in GAMMA. In this way, this project is quite successful, as we have identified several key areas where the GAMMA model could be improved. For example, Section 6 highlights the need to examine star-forming regions in more detail, and to implement more realistic models for nonuniform mixing

that are motivated by the hydrodynamical simulations. These models will be refined in future efforts by comparison to additional galaxies in the W12 simulations, and in more recent calculations like the Renaissance Simulations (O’Shea et al. 2015). Similarly, as future generations of physics-rich cosmological simulations add improved subgrid models for the ISM and star formation and feedback, this will result in updated physical prescriptions in our semi-analytic models.

One significant strength of directly comparing two different theoretical techniques, rather than using observations to calibrate the semi-analytical model, is that our validation methodology is unaffected by nuclear astrophysics and observational uncertainties. This is particularly important in terms of uncertainties relating to stellar modeling (see, e.g., Fields et al. 2018). Observationally, old stellar populations present a challenge when converting from integrated stellar spectra or color-color diagrams to metallicities and star formation rates, given uncertainties in stellar synthesis models and degeneracies between stellar age and metallicity (see, e.g., Conroy et al. 2009, 2010; Conroy & Gunn 2010). In the type of comparison we have undertaken, the hydrodynamical simulation provides these quantities with no uncertainty (although undoubtedly with inaccuracy, as described above and in the cited references). From a theoretical standpoint, stellar modeling is affected by uncertainties in nuclear reaction rates and in the physical prescriptions put into stellar evolution models (e.g., Young & Fryer 2007; Tur et al. 2009; Jones et al. 2015; deBoer et al. 2017; Nishimura et al. 2017). These both impose significant systematic uncertainties when comparing a hydrodynamical simulation or semi-analytical model to observations. When doing a model-to-model comparison such as we have undertaken, however, we can use the same underlying stellar models in both types of calculation and thus eliminate these sources of systematic uncertainty.

8.2. Current Limitations of GAMMA

The current version of GAMMA is limited in several ways in terms of its modeling assumptions. We did not include the contribution of Pop III stars, which probably affects our treatment of the lowest-metallicity stars in our models (Bromm et al. 2003; Wise et al. 2012b; Griffen et al. 2016). A single PopIII star explosion can create a metallicity floor of $[Z/H] \sim -3$ in the W12 simulation. One of the next steps is to include primordial stellar populations using a stochastic formation process similar to the one adopted in W12. We counted 13 Pop III remnants in the main target halo at the end of the simulation, which only represents $\sim 0.03\%$ of the

total stellar mass formed. The last Pop III star exploded at $t = 508$ Myr ($z = 9.7$).

Another limitation of **GAMMA** is its oversimplification of the gas phases. While the hydrodynamic simulation clearly shows multiphase interstellar and circumgalactic media with highly variable metallicity, our SAM only works with averaged quantities. The complexity of the interstellar medium should be included in **GAMMA**, but we first need to analyze the hydrodynamic simulation in more detail (see Section 8.4). We aim to improve **GAMMA** step-by-step where each new implementation is fully motivated and needed, as for the non-uniform mixing prescription (see Section 6).

Our SAM is also limited in terms of its analytical nature. Even if its complexity is increased, it will always provide a simplified representation of galaxies. For example, the stochastic (bursty) features and the rapid oscillation periods seen in the SFH of the W12 simulation is unlikely to be reproduced by **GAMMA**. Although the latter can generate oscillating behaviours (see the blue line in panel *d* of Figure 11), they are not driven by localized individual star formation bursts within the interstellar medium of the galaxy. They are rather caused by a periodic transfer of gas between the galaxy and the CGM (see, e.g., Stinson et al. 2007; Quillen & Bland-Hawthorn 2008; Côté et al. 2015; Muratov et al. 2015). In certain circumstances, because our models account for a delay between the formation of stars and the release of energy by SNe (see Equation 21), stars can accumulate enough *potential* energy to completely empty the galactic gas component. When the galactic outflow is launched, the galactic gas is transferred into the CGM and the star formation process is momentarily stopped, until part of the CGM gas falls back into the galaxy to start a new cycle.

Finally, we do not include yet the impact of an ionizing ultraviolet radiation background (UVB), which can prevent or limit star formation in dwarf galaxies after the reionization (e.g., Okamoto et al. 2008; Ma et al. 2017). Currently, if we were to run **GAMMA** beyond the reionization period down to redshift zero, our models would overestimate the stellar mass formed in low-mass galaxies. This UVB will be included in future work. We note that the W12 and Renaissance simulations include an H2-dissociating (Lyman-Werner) radiation background, but not an ionizing background. The ionizing radiation field is directly calculated by the radiation transport solver. Low-mass halos ($M_{\text{vir}} < 10^7 M_{\odot}$) are photo-evaporated from radiation, especially if they are near a galaxy.

8.3. Why Calibrate with Hydrodynamic Simulations?

Semi-analytic galaxy formation models targeting the nearby low-redshift universe primarily use observations for calibration, but some practitioners also use hydrodynamic simulations to inform them and to constrain their analytical prescriptions (e.g., Cattaneo et al. 2007; Saro et al. 2010; Stringer et al. 2010; Hirschmann et al. 2012; Neistein et al. 2012; Monaco et al. 2014; Guo et al. 2016; Mitchell et al. 2017). This approach is even more necessary when SAMs are targeting the early universe because the observational data available to constrain models are significantly less abundant and reduced in quality compared to the low-redshift universe.

The degeneracy highlighted in Section 7 suggests that it is unlikely that this type of modeling can constrain the physical processes which occur inside dwarf spheroidal and ultra-faint galaxies by only looking at their star formation history and stellar metallicity distribution functions. Technically, the observed age-metallicity relationship could break down our degeneracy (see Figure 11), but this relationship requires the determination of stellar ages which are uncertain by a factor of a few Gyr for the oldest stars (Bensby et al. 2014; Bergemann et al. 2014). In addition, the typical time bin for the star formation history in observed dwarf spheroidal galaxies is ~ 1 Gyr (Tolstoy et al. 2009; de Boer et al. 2012b,a, 2014; Weisz et al. 2014), which is a reflection of these uncertainties. This is large enough to hide the stochastic and bursty nature of the SFH at $z \gtrsim 7$.

At high redshift, observations are thus limited in their ability to constrain the physical processes implemented in SAMs. Adding stellar abundances in the list of constraints could help, but other constraints outside the realm of chemical evolution (e.g., gas fraction, star formation efficiency, gas flow rates) are the most valuable to break the degeneracy (Côté et al. 2017a). However, the Galactic halo and dwarf spheroidal and ultra-faint galaxies do not form stars anymore and cannot directly probe the physical conditions that led to their formation. In spite of the imperfection of cosmological hydrodynamic simulations (see Section 8.1), they still represent the best option to calibrate SAMs, since they are adequately resolved and provide crucial data that are otherwise unknown with observations.

8.4. Future Directions

The next step of this project is to extract further constraints from the W12 simulation. An important quantity to extract is the amount of gas involved in the star formation process, as it will allow us to constrain the star formation efficiency in **GAMMA** (see Figure 11). To create a consistent base for the comparison, we need

to define the star-forming region in the hydrodynamic simulation. This reservoir needs to include different gas phases in order to be representative of the simplified and averaged nature of the galactic gas in our SAM. However, the task is non-trivial since the spatial distribution of stars in the targeted high-redshift galaxy is complex and cannot be represented by a sphere or a rotating disk as in Mitchell et al. (2017). While the spatial distribution and the geometry of the star-forming region is not accounted for in our GAMMA models, they are important from the point of view of extracting the *correct* quantities from the hydrodynamic simulation.

Phase-space cuts (e.g., temperature, density, and metallicity thresholds) could be used to isolate the geometry of the star-forming region as a function of time, but we first need to better understand the metal recycling process within that central region. Indeed, we noticed that the hot metal-rich gas phase containing most the SNe ejecta has a very-short cooling timescale ($\lesssim 1$ Myr), which is below the time-resolution limit of our data outputs. At this stage, it is not clear whether this hot metal-rich gas efficiently mix with its surrounding before forming new stars. Deeper analysis is required, which possibly includes re-running parts of the simulation with higher temporal resolution to study the gas dynamics in more details.

In addition of isolating the mass of the star-forming region, inflowing and outflowing gas fluxes going through the star-forming region should be extracted from the simulation. These quantities would help to constrain the gas circulation process adopted in our SAM. Once the comparison framework between our semi-analytical models and high-redshift cosmological simulations is established, our plan is to repeat our experiment with the other galaxies found in the W12 simulation. The goal will be to derive general prescriptions that are valid for a wide range of galaxy masses. On the longer term, we will apply our methodology and inform GAMMA using the Renaissance simulations (O’Shea et al. 2015; Xu et al. 2016) in order to address a greater variety of galaxy formation environments in the early universe.

9. CONCLUSION

In this paper we presented GAMMA, our new semi-analytic galaxy formation model designed to address the origin of metal-poor stars and to reconstruct the chemical evolution history of low-mass galaxies in the early universe. A critical goal of this project is to calibrate our model by comparing its predictions with the ones extracted from high-redshift cosmological hydrodynamic simulations. In this paper, we targeted the most massive galaxy in the Wise et al. (2012a, referred to as W12)

simulation, extracted its mass assembly history (merger tree), and used it as an input in GAMMA to provide a consistent setup for comparing the semi-analytical and hydrodynamical approaches.

We found that GAMMA is able to reproduce the global trends predicted by the W12 simulation for the star formation history (SFH), the metallicity distribution function (MDF), and late stages of the age-metallicity relationship. However, there are degeneracies between the input parameters of GAMMA and it is not possible to constrain the star formation efficiency and the baryonic circulation processes using these constraints alone. Additional constraints such as the mass of gas involved in the star formation process need to be extracted from the hydrodynamic simulation to break the degeneracy (see Section 8.4).

Non-uniform mixing in the interstellar medium causes a broadening in the MDF, which can be emulated with GAMMA when convolving its MDF with Gaussian functions having a standard deviation of ~ 0.2 , a prescription motivated by the metallicity distributions of newly-formed stars seen in the hydrodynamic simulation at late times. However, some other features seen in the W12 simulation cannot be captured by GAMMA. This includes the stochasticity of the SFH and the sudden star formation events triggered by supernova explosions, which generate a non-negligible high-metallicity tail in the MDF. In addition, infalling satellite galaxies have active star formation, and tend to have outflows of metal-enriched gas while simultaneously falling into the halo of the targeted galaxy. This interaction between the satellite galaxies and the circumgalactic medium of the central galaxy is not included in the current version of our SAM.

The long-term goal of this project is to improve GAMMA to a point where it can provide valuable insights into the formation and evolution of local dwarf spheroidal and ultra-faint galaxies as well as the Galactic halo. This requires the derivation of galaxy evolution prescriptions that are general enough to be applicable to a wide range of galaxy masses and formation environments. To do so, we plan to repeat our experiment with more galaxies in the W12 simulation and ultimately extend our methodology to the Renaissance simulations (O’Shea et al. 2015; Xu et al. 2016).

We are thankful to the anonymous referee for providing constructive feedback and to Alex Ji, Falk Herwig, Brad Gibson, Hendrik Schatz, and Frank Timmes for their feedback on our paper prior submission. This research is supported by the National Science Foundation (NSF; USA) under grant No. PHY-1430152 (JINA Cen-

ter for the Evolution of the Elements) and by the ERC Consolidator Grant (Hungary) funding scheme (project RADIOSTAR, G.A. n. 724560). B.W.O. was supported by the National Aeronautics and Space Administration (NASA) through grant NNX15AP39G and Hubble Theory Grant HST-AR-13261.01-A, and by the NSF through grant AST-1514700. DS was supported by the NSF Astronomy and Astrophysics Postdoctoral Fellowship program. BDS is supported by NSF AST-1615848. JHW is supported by NSF grants AST-1333360 and AST-1614333, NASA grant NNX17AG23G, and Hubble theory grants HST-AR-13895 and HST-AR-14326.

Enzo and *yt* are developed by a large number of independent researchers from numerous institutions around the world. Their commitment to open science has helped make this work possible.

Software: *GAMMA* (this work), *OMEGA* (Côté et al. 2017a), *NuPyCEE* (Ritter & Côté 2016), *Enzo* (Bryan et al. 2014), *Rockstar* (Behroozi et al. 2013b), *ytree* (Smith et al., in preparation), *consistent-trees* (Behroozi et al. 2013c), *yt* (Turk et al. 2011), *grafic* (Bertschinger 2001), *Moray* (Wise & Abel 2011), *Grackle* (Smith et al. 2017), *NumPy* (Van Der Walt et al. 2011), *matplotlib* (<https://matplotlib.org>), *pydot* (<https://pypi.python.org/pypi/pydot>).

REFERENCES

- Abel, T., Anninos, P., Zhang, Y., & Norman, M. L. 1997, *New Astronomy*, 2, 181
- Abel, T., Bryan, G. L., & Norman, M. L. 2002, *Science*, 295, 93
- Agertz, O., & Kravtsov, A. V. 2016, *ApJ*, 824, 79
- Andrews, B. H., Weinberg, D. H., Schönrich, R., & Johnson, J. A. 2017, *ApJ*, 835, 224
- Anglés-Alcázar, D., Faucher-Giguère, C.-A., Kereš, D., et al. 2017, *MNRAS*, 470, 4698
- Anninos, P., Zhang, Y., Abel, T., & Norman, M. L. 1997, *New Astronomy*, 2, 209
- Atek, H., Richard, J., Kneib, J.-P., et al. 2014, *ApJ*, 786, 60
- Barkana, R., & Loeb, A. 2001, *PhR*, 349, 125
- Baugh, C. M. 2006, *Reports on Progress in Physics*, 69, 3101
- Beckwith, S. V. W., Stiavelli, M., Koekemoer, A. M., et al. 2006, *AJ*, 132, 1729
- Behroozi, P. S., Wechsler, R. H., & Conroy, C. 2013a, *ApJ*, 770, 57
- Behroozi, P. S., Wechsler, R. H., & Wu, H.-Y. 2013b, *ApJ*, 762, 109
- Behroozi, P. S., Wechsler, R. H., Wu, H.-Y., et al. 2013c, *ApJ*, 763, 18
- Bensby, T., Feltzing, S., & Oey, M. S. 2014, *A&A*, 562, A71
- Bergemann, M., Ruchti, G. R., Serenelli, A., et al. 2014, *A&A*, 565, A89
- Berger, M. J., & Colella, P. 1989, *J. Comp. Phys.*, 82, 64
- Bertschinger, E. 2001, *ApJS*, 137, 1
- Bland-Hawthorn, J., & Gerhard, O. 2016, *ARA&A*, 54, 529
- Bovill, M. S., & Ricotti, M. 2009, *ApJ*, 693, 1859
- Bower, R. G., Benson, A. J., Malbon, R., et al. 2006, *MNRAS*, 370, 645
- Bower, R. G., Vernon, I., Goldstein, M., et al. 2010, *MNRAS*, 407, 2017
- Boylan-Kolchin, M., Weisz, D. R., Johnson, B. D., et al. 2015, *MNRAS*, 453, 1503
- Bromm, V., Coppi, P. S., & Larson, R. B. 2002, *ApJ*, 564, 23
- Bromm, V., Yoshida, N., & Hernquist, L. 2003, *ApJL*, 596, L135
- Bryan, G. L., & Norman, M. L. 1997, ArXiv Astrophysics e-prints, [astro-ph/9710187](https://arxiv.org/abs/astro-ph/9710187)
- . 1998, *ApJ*, 495, 80
- Bryan, G. L., Norman, M. L., Stone, J. M., Cen, R., & Ostriker, J. P. 1995, *Comp. Phys. Comm*, 89, 149
- Bryan, G. L., Norman, M. L., O’Shea, B. W., et al. 2014, *ApJS*, 211, 19
- Bustard, C., Zweibel, E. G., & D’Onghia, E. 2016, *ApJ*, 819, 29
- Cattaneo, A., Blaizot, J., Weinberg, D. H., et al. 2007, *MNRAS*, 377, 63
- Chen, P., Wise, J. H., Norman, M. L., Xu, H., & O’Shea, B. W. 2014, *ApJ*, 795, 144
- Cohen, J. G., Christlieb, N., Thompson, I., et al. 2013, *ApJ*, 778, 56
- Conroy, C., & Gunn, J. E. 2010, *ApJ*, 712, 833
- Conroy, C., Gunn, J. E., & White, M. 2009, *ApJ*, 699, 486
- Conroy, C., White, M., & Gunn, J. E. 2010, *ApJ*, 708, 58
- Côté, B., Martel, H., & Drissen, L. 2015, *ApJ*, 802, 123
- Côté, B., O’Shea, B. W., Ritter, C., Herwig, F., & Venn, K. A. 2017a, *ApJ*, 835, 128
- Côté, B., Ritter, C., Herwig, F., et al. 2017b, in *14th International Symposium on Nuclei in the Cosmos (NIC2016)*, ed. S. Kubono, T. Kajino, S. Nishimura, T. Isobe, S. Nagataki, T. Shima, & Y. Takeda, 020203

- Côté, B., Ritter, C., O’Shea, B. W., et al. 2016a, *ApJ*, **824**, 82
- Côté, B., West, C., Heger, A., et al. 2016b, *MNRAS*, **463**, 3755
- Crosby, B. D., O’Shea, B. W., Beers, T. C., & Tumlinson, J. 2016, *ApJ*, **820**, 71
- Croton, D. J., Springel, V., White, S. D. M., et al. 2006, *MNRAS*, **365**, 11
- Croton, D. J., Stevens, A. R. H., Tonini, C., et al. 2016, *ApJS*, **222**, 22
- Davé, R., Finlator, K., & Oppenheimer, B. D. 2012, *MNRAS*, **421**, 98
- de Boer, T. J. L., Tolstoy, E., Lemasle, B., et al. 2014, *A&A*, **572**, A10
- de Boer, T. J. L., Tolstoy, E., Hill, V., et al. 2012a, *A&A*, **544**, A73
- . 2012b, *A&A*, **539**, A103
- deBoer, R. J., Gorres, J., Wiescher, M., et al. 2017, ArXiv e-prints, [arXiv:1709.03144](https://arxiv.org/abs/1709.03144) [nucl-ex]
- Fenner, Y., & Gibson, B. K. 2003, *PASA*, **20**, 189
- Fields, C. E., Timmes, F. X., Farmer, R., et al. 2018, *ApJS*, **234**, 19
- Finlator, K. 2017, in *Astrophysics and Space Science Library*, Vol. 430, *Astrophysics and Space Science Library*, ed. A. Fox & R. Davé, 221
- Fontanot, F., De Lucia, G., Hirschmann, M., et al. 2017, *MNRAS*, **464**, 3812
- Frebel, A., & Norris, J. E. 2015, *ARA&A*, **53**, 631
- Glover, S. C. O., & Abel, T. 2008, *MNRAS*, **388**, 1627
- Griffen, B. F., Dooley, G. A., Ji, A. P., et al. 2016, ArXiv e-prints, [arXiv:1611.00759](https://arxiv.org/abs/1611.00759)
- Guo, Q., Gonzalez-Perez, V., Guo, Q., et al. 2016, *MNRAS*, **461**, 3457
- Henriques, B. M. B., White, S. D. M., Thomas, P. A., et al. 2015, *MNRAS*, **451**, 2663
- . 2013, *MNRAS*, **431**, 3373
- Hirai, Y., Ishimaru, Y., Saitoh, T. R., et al. 2017, *MNRAS*, **466**, 2474
- Hirschmann, M., Naab, T., Somerville, R. S., Burkert, A., & Oser, L. 2012, *MNRAS*, **419**, 3200
- Hopkins, P. F., Kereš, D., Oñorbe, J., et al. 2014, *MNRAS*, **445**, 581
- Hopkins, P. F., Quataert, E., & Murray, N. 2011, *MNRAS*, **417**, 950
- . 2012, *MNRAS*, **421**, 3522
- Illingworth, G. D., Magee, D., Oesch, P. A., et al. 2013, *ApJS*, **209**, 6
- Ishigaki, M., Kawamata, R., Ouchi, M., et al. 2015, *ApJ*, **799**, 12
- Jones, S., Hirschi, R., Pignatari, M., et al. 2015, *MNRAS*, **447**, 3115
- Kim, H.-S., Baugh, C. M., Cole, S., Frenk, C. S., & Benson, A. J. 2009, *MNRAS*, **400**, 1527
- Kimm, T., Katz, H., Haehnelt, M., et al. 2017, *MNRAS*, **466**, 4826
- Komatsu, E., Smith, K. M., Dunkley, J., et al. 2011, *ApJS*, **192**, 18
- Komiya, Y., Yamada, S., Suda, T., & Fujimoto, M. Y. 2014, *ApJ*, **783**, 132
- Lacey, C. G., Baugh, C. M., Frenk, C. S., et al. 2016, *MNRAS*, **462**, 3854
- Lagos, C. D. P., Lacey, C. G., Baugh, C. M., Bower, R. G., & Benson, A. J. 2011, *MNRAS*, **416**, 1566
- Lu, Y., Kereš, D., Katz, N., et al. 2011, *MNRAS*, **416**, 660
- Lu, Y., Mo, H. J., Katz, N., & Weinberg, M. D. 2012, *MNRAS*, **421**, 1779
- Ma, X., Hopkins, P. F., Garrison-Kimmel, S., et al. 2017, ArXiv e-prints, [arXiv:1706.06605](https://arxiv.org/abs/1706.06605)
- Martin, C. L. 2005, *ApJ*, **621**, 227
- Mitchell, P. D., Lacey, C. G., Lagos, C. D. P., et al. 2017, ArXiv e-prints, [arXiv:1709.08647](https://arxiv.org/abs/1709.08647)
- Monaco, P., Benson, A. J., De Lucia, G., et al. 2014, *MNRAS*, **441**, 2058
- Muratov, A. L., Kereš, D., Faucher-Giguère, C.-A., et al. 2015, *MNRAS*, **454**, 2691
- Murray, N., Quataert, E., & Thompson, T. A. 2005, *ApJ*, **618**, 569
- Naab, T., & Ostriker, J. P. 2017, *ARA&A*, **55**, 59
- Neistein, E., Khochfar, S., Dalla Vecchia, C., & Schaye, J. 2012, *MNRAS*, **421**, 3579
- Nishimura, N., Hirschi, R., Rauscher, T., Murphy, A. S. J., & Cescutti, G. 2017, *MNRAS*, **469**, 1752
- Okamoto, T., Gao, L., & Theuns, T. 2008, *MNRAS*, **390**, 920
- O’Shea, B. W., & Norman, M. L. 2007, *ApJ*, **654**, 66
- O’Shea, B. W., Wise, J. H., Xu, H., & Norman, M. L. 2015, *ApJL*, **807**, L12
- Pawlik, A. H., Milosavljević, M., & Bromm, V. 2013, *ApJ*, **767**, 59
- Pignatari, M., Herwig, F., Hirschi, R., et al. 2016, *ApJS*, **225**, 24
- Pilkington, K., & Gibson, B. K. 2012, in *Nuclei in the Cosmos (NIC XII)*, 227
- Quillen, A. C., & Bland-Hawthorn, J. 2008, *MNRAS*, **386**, 2227
- Riebe, K., Partl, A. M., Enke, H., et al. 2013, *Astronomische Nachrichten*, **334**, 691

- Ritter, C., & Côté, B. 2016, NuPyCEE: NuGrid Python Chemical Evolution Environment, Astrophysics Source Code Library, [ascl:1610.015](#)
- Ritter, C., Herwig, F., Jones, S., et al. 2017, ArXiv e-prints, [arXiv:1709.08677 \[astro-ph.SR\]](#)
- Rodrigues, L. F. S., Vernon, I., & Bower, R. G. 2017, *MNRAS*, **466**, 2418
- Roederer, I. U., Preston, G. W., Thompson, I. B., et al. 2014, *AJ*, **147**, 136
- Romano, D., Bellazzini, M., Starkenburg, E., & Leaman, R. 2015, *MNRAS*, **446**, 4220
- Romano, D., & Starkenburg, E. 2013, *MNRAS*, **434**, 471
- Rosdahl, J., Katz, H., Blaizot, J., et al. 2018, ArXiv e-prints, [arXiv:1801.07259](#)
- Saro, A., De Lucia, G., Borgani, S., & Dolag, K. 2010, *MNRAS*, **406**, 729
- Scannapieco, C., Wadepuhl, M., Parry, O. H., et al. 2012, *MNRAS*, **423**, 1726
- Schaye, J., Dalla Vecchia, C., Booth, C. M., et al. 2010, *MNRAS*, **402**, 1536
- Schaye, J., Crain, R. A., Bower, R. G., et al. 2015, *MNRAS*, **446**, 521
- Simpson, C. M., Grand, R. J. J., Gómez, F. A., et al. 2017, ArXiv e-prints, [arXiv:1705.03018](#)
- Smith, B. 2018, <https://github.com/brittonsmith/ytree>: ytree version 2.0.2 release
- Smith, B. D., Bryan, G. L., Glover, S. C. O., et al. 2017, *MNRAS*, **466**, 2217
- Somerville, R. S., & Davé, R. 2015, *ARA&A*, **53**, 51
- Springel, V., White, S. D. M., Tormen, G., & Kauffmann, G. 2001, *MNRAS*, **328**, 726
- Starkenburg, E., Helmi, A., De Lucia, G., et al. 2013, *MNRAS*, **429**, 725
- Stinson, G. S., Dalcanton, J. J., Quinn, T., Kaufmann, T., & Wadsley, J. 2007, *ApJ*, **667**, 170
- Stringer, M. J., Brooks, A. M., Benson, A. J., & Governato, F. 2010, *MNRAS*, **407**, 632
- Tolstoy, E., Hill, V., & Tosi, M. 2009, *ARA&A*, **47**, 371
- Toro, E. F. 1997, Riemann solvers and numerical methods for fluid dynamics : a practical introduction (Berlin, New York: Springer)
- Truelove, J. K., Klein, R. I., McKee, C. F., et al. 1998, *ApJ*, **495**, 821
- Tumlinson, J. 2006, *ApJ*, **641**, 1
- . 2010, *ApJ*, **708**, 1398
- Tur, C., Heger, A., & Austin, S. M. 2009, *ApJ*, **702**, 1068
- Turk, M. J., Abel, T., & O’Shea, B. 2009, *Science*, **325**, 601
- Turk, M. J., Smith, B. D., Oishi, J. S., et al. 2011, *ApJS*, **192**, 9
- Van Der Walt, S., Colbert, S. C., & Varoquaux, G. 2011, ArXiv e-prints, [arXiv:1102.1523 \[cs.MS\]](#)
- Vincenzo, F., Matteucci, F., de Boer, T. J. L., Cignoni, M., & Tosi, M. 2016, *MNRAS*, **460**, 2238
- Vogelsberger, M., Genel, S., Springel, V., et al. 2014, *MNRAS*, **444**, 1518
- Weinberg, D. H., Andrews, B. H., & Freudenburg, J. 2017, *ApJ*, **837**, 183
- Weisz, D. R., & Boylan-Kolchin, M. 2017, *MNRAS*, **469**, L83
- Weisz, D. R., Dolphin, A. E., Skillman, E. D., et al. 2014, *ApJ*, **789**, 147
- White, S. D. M., & Frenk, C. S. 1991, *ApJ*, **379**, 52
- Williams, R. E., Blacker, B., Dickinson, M., et al. 1996, *AJ*, **112**, 1335
- Wise, J. H., & Abel, T. 2011, *MNRAS*, **414**, 3458
- Wise, J. H., Abel, T., Turk, M. J., Norman, M. L., & Smith, B. D. 2012a, *MNRAS*, **427**, 311
- Wise, J. H., Demchenko, V. G., Halicek, M. T., et al. 2014, *MNRAS*, **442**, 2560
- Wise, J. H., Turk, M. J., Norman, M. L., & Abel, T. 2012b, *ApJ*, **745**, 50
- Woodward, P. R., & Colella, P. 1984, *J. Comp. Phys.*, **54**, 174
- Xu, H., Wise, J. H., Norman, M. L., Ahn, K., & O’Shea, B. W. 2016, *ApJ*, **833**, 84
- Yates, R. M., Henriques, B., Thomas, P. A., et al. 2013, *MNRAS*, **435**, 3500
- Young, P. A., & Fryer, C. L. 2007, *ApJ*, **664**, 1033